Sustainable fabrication of piezoceramic-rich and graphene-based composites for fully 3D-printed flexible sensors

Smart Materials and Structures

OPEN ACCESS

RECEIVED
18 March 2026

REVISED
9 July 2026

ACCEPTED FOR PUBLICATION
19 July 2026

PUBLISHED
30 July 2026

PAPER

Sustainable fabrication of piezoceramic-rich and graphene-based composites for fully 3D-printed flexible sensors

Gopi Kompelli[1], Rolanas Dauksevicius[1,*], Šarūnas Svirskas[2], Elena Jasiūnienė[3,4], Vaidotas Cicenas[3] and Roman Turczyn[5,6]

[1] Institute of Mechatronics, Kaunas University of Technology, Studentu str. 56, LT-51424 Kaunas, Lithuania
[2] Faculty of Physics, Vilnius University, Sauletekio 3, LT-10257 Vilnius, Lithuania
[3] Prof. K. Barsauskas Ultrasound Research Institute, Kaunas University of Technology, K. Barsausko str. 59, LT-51423 Kaunas, Lithuania
[4] Department of Electronics Engineering, Kaunas University of Technology, Studentu str. 50, LT-51368 Kaunas, Lithuania
[5] Department of Physical Chemistry and Technology of Polymers, Silesian University of Technology, Strzody 9, 44-100 Gliwice, Poland
[6] Centre for Organic and Nanohybrid Electronics, Silesian University of Technology, Konarskiego 22B, 44-100 Gliwice, Poland
[*] Author to whom any correspondence should be addressed.

E-mail: rolanas.dauksevicius@ktu.lt

Keywords: FDM, thermoplastic, nanocomposite, percolation, piezoelectricity, polarization, hysteresis

Supplementary material for this article is available online

Abstract

Progress in additively manufactured piezoelectrics is impeded by environmental, regulatory and scalability concerns related to solvent processing. Hazardous solvents dominate the preparation of polyvinylidene fluoride (PVDF)-based piezocomposites for fused filament fabrication (FFF), which remains underdeveloped compared to solvent-assisted additive electronics technologies. The piezoelectric performance of existing FFF-printed PVDF composites is limited due to moderate ferroelectric ceramic content ($\lesssim$35 vol%). Solvent-free processing and multi-material FFF of highly ceramic-filled ($\gtrsim$50 vol%) piezoelectric devices are largely underexplored. Herein, we report the fully melt-based fabrication of a flexible lead-free piezocomposite filament, highly filled with barium titanate (BTO) particles at the upper printability threshold (∼55 vol%), enabling FFF of piezoelectric sensors with co-printed graphene-doped electrodes. X-ray microtomography and tensile testing indicate that re-extrusion provides uniform filler dispersion in a soft PVDF copolymer (PVDF-HFP) matrix. The multi-material FFF process is fine-tuned to deliver consistent 3D printing of well-fused ceramic-rich and graphene-doped sheets as indicated by strain-rate strengthening behavior. Adding 8 wt% graphene nanoplatelets yields 1.6 S cm^{-1} conductivity and $<$100 Ω/sq sheet resistance, sufficient for effective strong-field poling ($\gtrsim$20 kV mm^{-1}). The achieved maximum values of d_{33} (35.4 pC/N) and dielectric constant (108 at 1 kHz) are comparable to or exceed solvent-processed counterparts, aligning with predictions of effective medium models. The 3D-printed vibration sensors exhibit practically usable d_{31}-mode sensitivity with high linearity and repeatability, confirming FFF reproducibility. This study establishes a scalable and cost-effective solvent-free process for environmentally responsible material extrusion additive manufacturing of flexible piezoelectric devices, addressing current limitations in composite filling level and processing sustainability.

1. Introduction

Advances in printed electronics impact the progress in additively manufactured piezo-electronics (AMPE) [1], which also intersects with the emerging field of 4D printing [2]. Development of printable electroactive (piezoelectric, conductive, etc) materials and their adaptation for multi-material AM processes represents a viable pathway to produce customized piezo-devices (mechanical sensors, nanogenerators, ultrasonic transducers, sensorized implants, etc [1–3]). AMPE systems are widely applicable,

including biomedical devices [4], smart wearables, robotics and structural health monitoring platforms [5]. These performance-critical piezoelectric applications commonly rely on durable, (bio)stable and ferroelectric PVDF-based polymers [6]. They are resistant to hydrolytic degradation and long-term exposure to physiological fluids as well as to many harsh chemicals, weathering, corrosion, ignition and abrasion [7]. PVDF-based piezo-devices are printed by various methods that are predominantly implemented using solvent-assisted approaches (e.g. casting, screen printing), including more sophisticated ink jetting, spraying or writing processes (e.g. inkjet, aerosol jet, E-jet, DIW) [2].

Fused filament fabrication (FFF) became one of the mainstream methods for MEX AM of thermoplastic parts. Similar to FFF, fused granulate fabrication (FGF) undergoes a rise in adoption, particularly in large-format AM. FFF of piezo-devices started gaining momentum a decade ago [8]. It was first applied earlier for printing ceramic green parts using extrudable piezoceramic-binder (polymer-bound) feedstock [9]. Generally, FFF is more accessible compared to ink-based methods, which rely on complex-rheology ink/paste formulations and usually involve post-print curing or sintering. The availability and affordability of FFF/FGF hardware and feedstock is continuously improving, which facilitates democratization of 3D/4D printing [2]. Furthermore, FFF/FGF processes are more easily adaptable to large-format AM implementations [10]. Development of multi-material MEX AM capabilities is a key objective for enabling efficient single-process printing of monolithic piezo-devices, including additive *in-situ* embedding into other components via co-printing of structural and electroactive materials [2] (e.g. for strain and force sensing [5]). With further research efforts, multi-material MEX AM could become a viable AMPE technology for rapid prototyping and on-demand manufacturing of customized piezo-devices [1, 2, 5].

A typical piezo-device (e.g. vibration sensor or energy harvester) requires monolithic integration of diverse functional layers such as piezoelectric, conductive, insulating and encapsulating [2, 5]. The field of FFF-printed piezo-devices is in its infancy since prior studies were mainly concerned with the fabrication of piezo-material filaments and printing of piezo-sheets. PVDF is the most widely studied piezopolymer [1, 2], including the field of FFF [11–18], where the focus remains on optimization of extrusion-induced crystallization to enhance formation of electroactive phases [19]. Most works on FFF-printed PVDF relied on solvent-free fabrication of filaments by applying hot melt extrusion (HME) of the homopolymer pellets [11–17]. However, the electrodes were typically formed using non-additive methods (table S1), which are hardly amenable to the implementation of cost-efficient AMPE workflows. The printed piezo-sheets were usually electroded with conductive pastes and foils. Few research groups implemented a single-process FFF workflow to fully print a piezo-device as a monolithically electroded piezo-sheet (piezopolymer-based [20–22] and piezocomposite-based [23–25] materials were used). They were usually printed with commercial-off-the-shelf (COTS) filaments, which were used to form piezo-sheets [16, 17, 26], electrodes [25] or both [20, 22]. In several works, a hybrid AM approach was adopted, where FFF was combined with another MEX method (e.g. DIW [26]). Such integrated approaches continue to advance and will improve AMPE functionality and versatility [5]. However, hybrid AMPE manufacturing requires more sophisticated industrial-grade infrastructure [27], particularly when complex inks containing hazardous solvents must be handled safely. Therefore, such requirements may complicate piezo-device printing for budget-constrained users and impede their access to the AMPE field.

Piezocomposite filaments were mostly produced by mixing with non-aqueous solvents that present various environmental and health risks. Hazardous polar aprotic solvent DMF was widely used [28–36] (table S1) despite it being classified as a substance of very high concern due to reprotoxic effects [37, 38]. Processing with less hazardous solvents appears to be the exception in this case (e.g. acetone [39]). Overall, in addition to regulatory and safety concerns, solvent-assisted fabrication imposes severe constraints on scalability since dedicated facilities are required for wet-processing operations such as homogenization, casting, evaporation and solvent recovery [40, 41]. Studies on solvent-free fabrication of piezocomposite filaments are less common (table S1), while the electrodes in this case were mostly formed non-additively [42–45]. It is noted that reports on solvent-free in-house fabrication and printing of both piezoelectric and conductive filament are scarce. Neat PVDF and CNT-filled conductive filaments were extruded in [21], while in [25] a lead-based piezocomposite filament was fabricated via a melt-based workflow, though a COTS conductive filament was used.

Most piezocomposite filaments were developed by combining PVDF homopolymer and lead-free piezoceramic fillers (table S1). Barium titanate (BTO) particles were mostly used since they offer a favorable balance between cost and piezoelectric performance together with diverse industrial and biomedical applicability [46]. Other piezoceramic fillers were rarely used (e.g. KNN-based [24, 30, 36], ZnO [47]). The semi-rigid PVDF is a relatively stiff matrix material that compromises composite flexibility when a

larger piezoceramic content is added. Softer matrix materials were rarely employed in FFF-printed piezo-composites (e.g. PVDF-HFP copolymer [24, 30, 48], elastomers [25]). Table S1 shows that piezoceramic content was typically limited to $\lesssim$40 wt% and rarely exceeded $\gtrsim$50 wt% (up to 35 vol% [24, 36]), while cases of $\gtrsim$70 wt% ($\gtrsim$40 vol%) were possibly never reported for the FFF-based piezo-devices. In contrast, higher ceramic content of up to ∼50–60 vol% was reported in solvent-processed non-piezoelectric composites (printed [49], solvent-cast [50–52]) and in molded piezocomposites [53–55] (including solvent-free [54]). This indicates that melt-based processability and printability limits have not been achieved so far since prior studies on FFF-based piezocomposites employed moderate filling levels (table S1). Electrodes were mostly formed using conductive filaments with carbon nanomaterials [20, 21, 23–25], while metallic fillers were rarely used [22].

The adoption of HME- and MEX-based workflows for solvent-free additive manufacturing of piezocomposite-based devices is in an early research phase. Compared to unfilled or lower-filled polymers, the melt-based fabrication of highly filled composites ($\gtrsim$50 vol% filling level [56]) is more demanding due to increased melt viscosity and filler agglomeration [57]. In FFF printing, it may destabilize melt flow, promote nozzle clogging [25] and lead to inconsistent melt deposition and weaker fusion zones with micro-defects [48]. The efficiency of piezocomposite printing and electrical poling strongly depends on filler dispersion homogeneity [58]. Poorly dispersed filler state translates into less effective poling by causing premature dielectric breakdown at weaker electrical fields, which results in unsatisfactory piezoelectric properties [59]. Filler homogenization during solvent-free fabrication of (electroactive) composites often relies on specialized melt processing equipment that is hardly affordable to budget-constrained users (e.g. shear mixers [44, 45], twin-screw extruders [25, 42, 43] or other compounders [60]).

To address these limitations, there is a need to develop more sustainable, cost-efficient and scalable processing routes [61] to alleviate technological complexities in MEX AM of piezo-devices. Our study presents a solvent-free re-extrusion/granulation process to produce filaments of highly piezoceramic-filled composite and graphene-doped conductive composite for 3D printing of a flexible electromechanical sensor. It is based on a piezocomposite with ∼55 vol% BTO fraction, which is ∼1.5–2 times higher than commonly reported ($\lesssim$35 vol%, table S1). The approach represents an affordable, scalable and greener alternative to the solvent-assisted routes as similar studies on solvent-free manufacturing of ceramic-rich piezocomposite filaments and FFF-printing of monolithically electroded piezoelectric sensors are scarce (possibly a single published report [25], where a lower content of lead-based piezoceramic was used). In our work, a budget-friendly extruder and FFF machine are used to produce and print the highly filled PVDF-HFP/BTO filament and conductive graphene-doped PVDF-HFP filaments. A multi-material FFF workflow is implemented for co-printing piezocomposite and conductive sheets to form a monolithically electroded sensor. Micro-CT is used to analyze the distribution and morphology of air voids and filler agglomerates in the extruded filaments. Mechanical, dielectric, ferroelectric and piezoelectric properties of printed piezocomposites are determined. The study examines how poling history affects dielectric and ferroelectric responses, which possibly was never addressed earlier for the FFF-printed piezocomposites. The impact of wide-ranging poling fields and durations on d_{33} piezoresponse is evaluated to assess the feasibility of monolithically FFF-printed piezo-devices.

2. Fabrication and characterization of electroactive composites

2.1. Materials

PVDF-HFP powder Kynar Superflex® 2501–20, kindly donated by Arkema via distributor Labochema LT, has a melt flow rate of 2–14 g per 10-minute test period under 232 °C and 3.8 kg, melting temperature of 117 °C–125 °C and density of 1.79 g cm^{-3}. Pristine BTO powder (Inframat Advanced Materials LLC, USA, product No. 5622-ON5) consists of untreated spheroidal submicron particles (density of 5.85 g cm^{-3}, nominal average diameter of 0.5 μm). Flaky graphene powder (The Sixth Element (Changzhou) Materials Technology Co., Ltd, China, product No. SE1233) consists of graphene nanoplatelets (GNPs) having median size of ∼11 μm, specific surface area of ∼504 m^2 g^{-1} and tap density of ∼0.016 g cm^{-3}. No additional treatment or functionalization was performed for the materials before filament manufacturing.

2.2. Manufacturing of PVDF-HFP composite filaments

The filaments of highly filled piezocomposite and graphene-doped conductive composites were manufactured using a re-extrusion workflow with in-process filament granulation (figure 1). Due to high

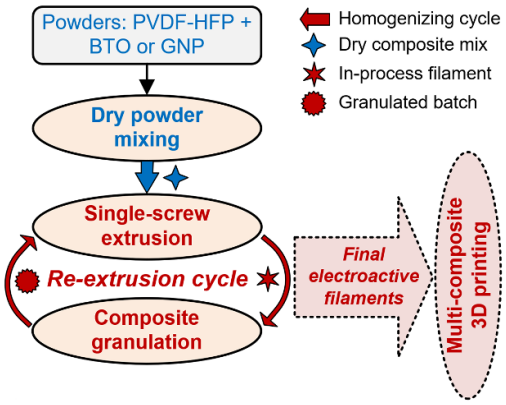

Figure 1. Re-extrusion/granulation process for solvent-free manufacturing of electroactive composite filaments.

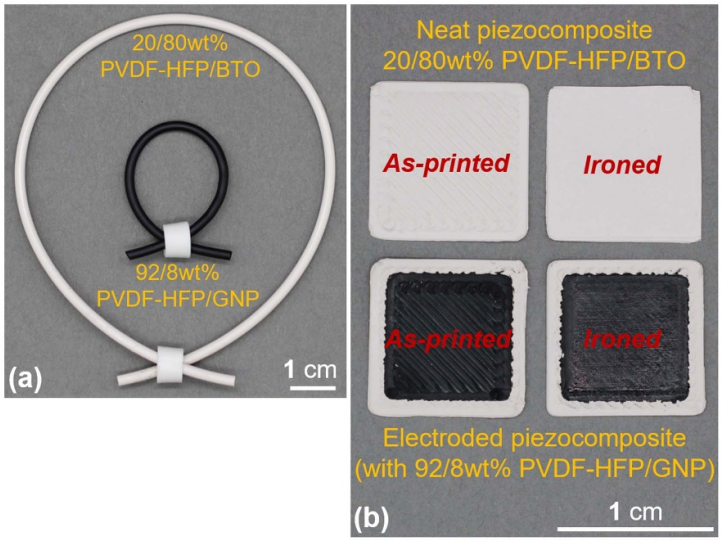

Figure 2. (a) Extruded flexible filaments of highly ceramic-filled piezocomposite and graphene-doped conductive composite. (b) Printed thin-sheet samples of neat and electroded piezocomposite (ironed samples were used for contact poling).

thermal stability, PVDF may be remelted at least 3 times without degradation of mechanical properties [48]. Therefore, the triple-extruded filaments were utilized for the initial prototyping and compositional feasibility trials. The primary objective was to maximize BTO or GNP content by balancing printability and functional performance to enhance piezoresponse or conductivity and retain satisfactory flexibility of the filaments and thin-sheet prints. Our previous study on filaments with more rigid PVDF-HFP and 20–60 wt% BTO [48] suggested that the objective could be reached by increasing BTO content from 60 to ∼80–85 wt% when using highly compliant Kynar Superflex® grade. Initial prototyping with 80 wt% BTO showed that the filament had acceptable flexibility (figure 2(a)) and could be reliably printed by effectively fine-tuning the FFF process (section 2.3). Extrusion tests were also conducted in 82–85 wt% BTO range, revealing that the filaments became increasingly rigid and brittle (e.g. spooling of the filament with 85 wt% ceramic was not possible). Moreover, FFF process reliability was insufficient to ensure disruption-free printing of numerous reproducible samples for mechanical and piezoelectric studies.

Initial prototyping tests with the graphene-doped filaments were conducted in 2–12 wt% GNP range. Percolation was known to occur below ∼3 wt% [62] and functionally usable conductivity levels were expected at ∼8 wt% GNP [63]. The filaments with 10 and 12 wt% GNP were excluded from further testing due to limited flexibility and excessive melt viscosity, which caused erratic clogging during printing. In contrast, despite high flexibility and consistent printability, the conductivity was found to be unsatisfactory at 2 and 4 wt% GNP (section 3.4.3). The filament with 8 wt% GNP provided a suitable balance between conductivity, flexibility (figure 2(a)) and printability (section 2.3).

Table 1. Labels of the tested composite samples.

Label	Description of composition and processing
F*i*-BTO80	Filaments of 20/80 wt% PVDF-HFP/BTO piezocomposite extruded $i = 1 - 3$ times.
P*i*-BTO80	Prints of 20/80 wt% PVDF-HFP/BTO (printed with filaments extruded $i = 1 - 3$ times).
F*i*-GNP*j*	Filaments of PVDF-HFP composite with $j = 2/4/8$ wt% GNP extruded $i = 1 - 3$ times.
P*i*-GNP*j*	Prints of PVDF-HFP composite with $j = 2/4/8$ wt% GNP (printed with F*i*-GNP*j* filaments).
P–ES	Electroded piezocomposite (sensor) printed with F3-BTO80 and F3-GNP8 ($h_{piezo} \approx 0.5$ mm, $h_{el\text{-}bottom} \approx 0.1$ mm, $h_{el\text{-}top} \approx 0.12$ mm (ironed)).

Based on these initial findings, the single-, double- and triple-extruded filaments of 20/80 wt% PVDF-HFP/BTO and 92/8 wt% PVDF-HFP/GNP (table 1) were selected to examine the impact of re-extrusion on filament microstructural morphology (section 3.1) and determine tensile properties of printed composites (section 3.3). At the start of the re-extrusion/granulation workflow (figure 1), the pre-mixed powdered composite feedstock was extruded either into final (single-extruded) filament for printing or into in-process filament for granulation and repeated extrusion. An in-house built pelletizer was used to produce ∼2 mm granules. The effective temperatures for the two heating zones of a single-screw extruder Noztek Touch were determined through multiple extrusion trials (1.75 mm nozzle was used). The objective was to minimize melt processing temperature for reduced thermal impact on the polymer and to ensure sufficient filament quality for a more consistent FFF process. A reverse temperature profile was selected by setting 180 °C for the barrel zone and 170 °C for the nozzle. Slightly higher barrel temperature was required to operate the motor within torque limits and to suppress motor speed fluctuations when processing highly viscous melts (stable filament extrusion was achieved at 40–50 RPM). A higher extrusion throughput of ∼300 mm min^{-1} was achieved for the piezocomposite filament compared to the ∼150 mm min^{-1} for the conductive counterpart (measured during re-extrusion cycles). The extruder was installed at 45°, allowing the filament to be continuously tensioned via gravitational pull. Forced air cooling was applied near the nozzle to control the solidification rate of the extrudate and prevent excessive diameter reduction in the gravity-tensioned filament. This approach maintained the dimensional accuracy of filaments within the acceptable tolerance (⌀1.75 ± 0.1 mm) to ensure reproducible FFF. Filament diameter was measured at 1.707 ± 0.011 and 1.709 ± 0.013 mm for the piezoelectric and conductive composites, respectively.

2.3. Multi-material 3D printing workflow

A single-printhead FFF machine Prusa i3 MK3S was used to print neat (unelectroded) PVDF-HFP/BTO samples and their electroded counterparts, where the piezocomposite sheet is sandwiched between printed conductive PVDF-HFP/GNP sheets (figure 2(b)). To achieve stable printing, the printer was upgraded with Slice Engineering® Copperhead® components to enhance thermal performance at the hotend (e.g. more uniform temperature distribution, lower heat creep, enhanced insulation). A Fibtip tool-steel nozzle was customized by enlarging its bore diameter from 0.6 to 1.2 mm to ensure an uninterrupted clogging-free FFF process. Due to higher viscosity, the PVDF-HFP/GNP composite was prone to clogging with nozzles smaller than 1 mm. Table 2 summarizes the main printing parameters and conditions identified as most effective for manufacturing consistency and print quality.

To increase composite melt flowability, a higher nozzle temperature of 260 °C was used during FFF (temperature at filament extruder nozzle was 180 °C). Due to higher printing temperature the nozzle clogging risks were suppressed, providing uniform deposition of the composite melts on the build plate. The Kapton tape was attached to the build plate to facilitate sample removal. A thin coating of Dimafix® adhesive was applied on the Kapton tape, while the build plate was heated to 70 °C to prevent print detachment. A reduced printing speed of 10 mm s^{-1} was required to minimize the risk of FFF disruptions and print defects when using abrasive ceramic-rich piezocomposite filaments. The total printing duration for the tensile test samples (section 2.5) was approximately 15 and 24 min for the neat and electroded piezocomposite samples, respectively.

A larger extrusion multiplier of 1.3 was applied to prevent flow rate fluctuations, under-extrusion defects, geometric distortions and dimensional deviations (nonuniform layer height, air voids). The reduced extrusion width of 1.0 mm was selected for the 1.2 mm nozzle to enhance bonding between the tracks by effectively laminating them and mitigating print defects. However, the increase in extrusion flow rate and the reduction in extrusion width resulted in ridges forming on the top surface. Therefore, the as-printed poling samples (figure 2(b)) were additionally subjected to FFF finishing procedure (ironing) to smoothen the print surface and reduce structural imperfections. The ironing was observed to

Table 2. Specification of the multi-material FFF workflow.

Parameters	Printed electroactive composites	
	Ceramic-rich PVDF-HFP	Graphene-doped PVDF-HFP
Nozzle material, size	Tool steel, ⌀1.2 mm	
Printing temperature T_p	260 °C	
Bed temperature T_{bed}	70 °C	
Build surface	Smooth PEI + Kapton tape + Dimafix®	
Printing speed v_p	10 mm s^{-1}	5 mm s^{-1}
Extrusion multiplier	1.3	2
Extrusion width w_{extr}	1.0 mm	
Raster angle, infill	+45°/–45°, 100%	
Layer height (fan use)	0.1 mm (off)	
Ironing temperature T_{ir}	260 °C	
Ironing speed v_{ir}	10 mm s^{-1}	
Ironing angle, flow rate	90°, 0	
Ironing pass spacing	0.1 mm	

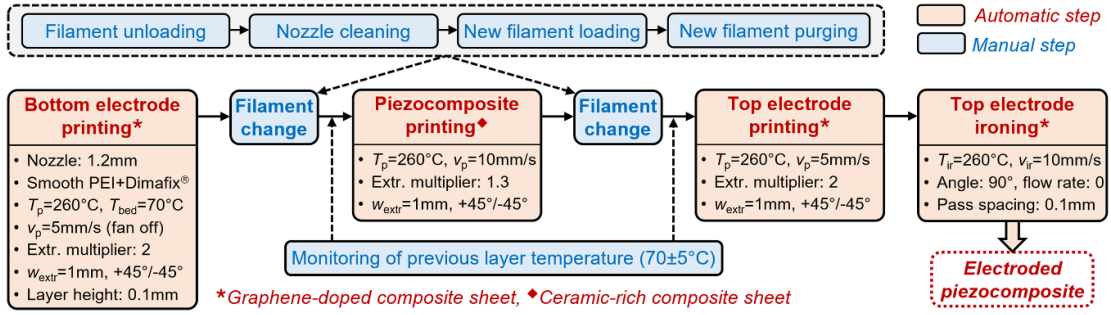

Figure 3. Multi-material single-printhead FFF workflow for co-printing filaments of highly ceramic-filled piezocomposite and graphene-doped conductive composite to additively manufacture piezoelectric sensors (the workflow is based on table 2).

mitigate the risk of dielectric breakdown during electrical poling experiments since air voids (micropores) and other print defects are detrimental to poling efficiency [59]. Ironing flow rate was disabled in PrusaSlicer 2.8.0 since the excess material (the ridges) was already present on the print surface. The ironing temperature and speed values were kept the same as in printing (260 °C, 10 mm s^{-1}), while the spacing between the ironing passes was set to a relatively low value of 0.1 mm.

The electroded piezocomposite (figure 2(b)) is a triple-sheet structure that comprises three individual sheets consisting of 8 printed layers in total: 5 layers for the piezocomposite sheet that is sandwiched between the single-layer bottom electrode and the double-layer top electrode sheets. The electroded piezocomposites were printed by implementing the multi-material FFF workflow (figure 3). It commenced with the deposition of PVDF-HFP/GNP electrode layer of ∼0.1 mm height. Next, the filament was manually changed to the PVDF-HFP/BTO one to print the 5-layer piezocomposite sheet of ∼0.5 mm height. Afterwards, the filament was changed again to print the double-layer top electrode of ∼0.2 mm height. The thicker top sheet was needed for the effective ironing step that smoothened the top electrode (figure 2(b)) and reduced its thickness to ∼0.12 mm. During filament changeovers, the hotend and nozzle were cleaned with a ⌀1 mm clog poke to push out the outgoing composite material, followed by purging ∼5 cm of the incoming filament to prevent contamination of the subsequent print layer. A non-contact thermometer was used to monitor and control the temperature of the preceding printed sheet. It was sufficient to maintain it within 70 ± 5 °C to prevent delamination by ensuring strong bonding between the fused sheets of different composites. A larger extrusion multiplier of 2 was required to increase the flow rate during electrode printing because of the inferior melt flowability of the conductive composite. In addition, a lower printing speed of 5 mm s^{-1} was specified to ensure consistent deposition of more viscous PVDF-HFP/GNP melt (suboptimal interlayer bonding was observed at a higher speed of 10 mm s^{-1} due to under-extrusion). The adjustments in FFF parameters for printing the electroded piezocomposites were executed through customized G-codes using PrusaSlicer 2.8.0. Due to differences in FFF parameters for both composites (table 2), it was necessary to enter the corresponding specific G-codes before printing the subsequent composite sheet atop the preceding one.

2.4. Contact poling and electrical characterizations

Printed neat and electroded piezocomposites were poled in silicone oil at 60 °C using high-voltage power supply Spellman SL600 (figure S1). Poling temperature of 60 °C was determined to be effective for similar composites [48]. All piezocomposite sheets (10 × 10 × 0.5 mm^3) were covered with a copper foil of 50 μm thickness. For the electroded piezocomposites, the foil was attached on the printed PVDF-HFP/GNP electrodes of a smaller area (∼5 × 5 × 0.1 mm^3) to prevent short circuiting and arcing as it is one of the failure risks [20]. After poling, the samples were removed from the heated oil for d_{33} measurements (3 samples per poling case were tested). A Berlincourt-type d_{33} meter PolyK PKD3-2000-F10N was employed with a force sensor to apply the static preload of 4 N and the dynamic compressive force of 0.25 N at 110 Hz (figure S1). Electromechanical sensing performance under bending (d_{31} operating mode) was evaluated with a shaker-based setup (figure S2) by recording piezocomposite sensor signals using a digital oscilloscope PicoScope 4824 via a custom-built transimpedance amplifier (gain: 1 mV nA^{-1}). It was connected to the printed sensors (40 × 13.5 × 0.72 mm^3) adhesively bonded on a host cantilever, which was subjected to flexural resonant excitation (figure S2) using an electrodynamic shaker with closed-loop vibration control B&K LDS V555-PA1000L-FPS10L-Type7542.

Dielectric and ferroelectric characterizations were performed at RT on piezocomposite samples (∼15 × 2 × 0.1 mm^3) printed as single tracks (i.e. without interfacial fusion zones), which were poled using 20 and 40 kV mm^{-1} DC field. Thin-film silver electrodes (∼300–350 nm) were evaporated on the poled single-track samples for the measurements. Dielectric spectra were determined by the conventional parallel-plate capacitor method. The LCR meter HP 4284 A was used to measure capacitance and loss tangent for deriving the real and imaginary parts of permittivity (V_{AC} = 1 V). Polarization–electric field (*P*–*E*) and displacement–electric field (*D*–*E*) hysteresis loops were measured with the ferroelectric analyzer AixACCT TF2000 by applying saw-shaped voltage waveform of different frequency in the 10–50 Hz range. Piezocomposite polarization was evaluated by integrating the measured current and dividing it by the sample area. The displacement was measured by the single-beam laser interferometer of the TF2000 analyzer. Conductivity of PVDF-HFP/GNP filament (100 mm length) was determined with Keithley SMU 2614B in four-point probe configuration at RT (filament ends were coated with silver paint). Sheet resistance of printed electrodes was measured with Ossila Four-Point Probe.

2.5. Mechanical testing

Printed thin strips of 150 × 10 × 0.5 mm^3 and 150 × 10 × 0.7 mm^3 were used as tensile test samples for the neat and electroded piezocomposites, respectively. The quasi-static testing was conducted at speeds of 10, 100 and 1000 mm min^{-1} (average engineering strain rates of 0.0033, 0.033 and 0.33 s^{-1}, respectively, for the extensometer gauge length of 50 mm). The strips correspond to type 2 samples in ISO 527–3 and were selected since piezoelectric and conductive materials are typically integrated as thin sheets into sensors or nanogenerators. Five samples were tested to determine average tensile strength and modulus, yield and fracture strains. The strength was derived as the ratio of the first force peak and the initial area of sample cross section. Tensile modulus was evaluated as the slope of the secant line between the strains of $\varepsilon_1 = 0.0005$ and $\varepsilon_2 = 0.0025$ according to equation $(\sigma_2 - \sigma_1)/(\varepsilon_2 - \varepsilon_1)$, where σ_1 and σ_2 are stresses corresponding to the strain values. The tests were performed at RT on the UTM Tinius Olsen H25KT using a 25 kN load cell. The samples were clamped in manual wedge action grips as per ISO 527–3. Strains were measured by tracking displacements of 3 gauge-mark pairs through a video extensometer Tinius Olsen VEM300.

2.6. Nondestructive evaluation with micro-CT

Micro-CT system RayScan 250E was used to perform 3D imaging and analysis of the composite filaments to characterize micro-defects (filler agglomerates and air voids). The scanning was conducted in the micro-focus mode by applying 160 kV voltage and current of 80 μA (for PVDF-HFP/BTO) and 120 μA (for PVDF-HFP/GNP). A total of 1800 projections of high resolution (voxel size—7 μm) were acquired for each sample with 2000 ms integration time. The spatial morphology of the micro-defects was characterized by their volume and surface areas, estimated by summing all the voxels assigned to the micro-defects. The morphology was evaluated using the Wadell's true sphericity index $S_W = A_s/A = \sqrt[3]{36\pi V^2}/A$ (A_s—surface area of a sphere with the same volume as the measured agglomerate that has actual surface area A and volume V) [64]. The index quantifies the extent of shape irregularity as a deviation from a perfect sphere (due to elongation, flattening, angularity, etc). $S_w = 1$ corresponds to a perfect sphere, $S_w \approx 0.9$–0.99 represents a nearly spherical shape, $S_w \approx 0.6$–0.9 indicates a moderately irregular shape (e.g. elongated, angular), and $S_w \lesssim 0.5$–0.6 corresponds to strongly irregular morphology (e.g. flattened disk-like shapes) [65].

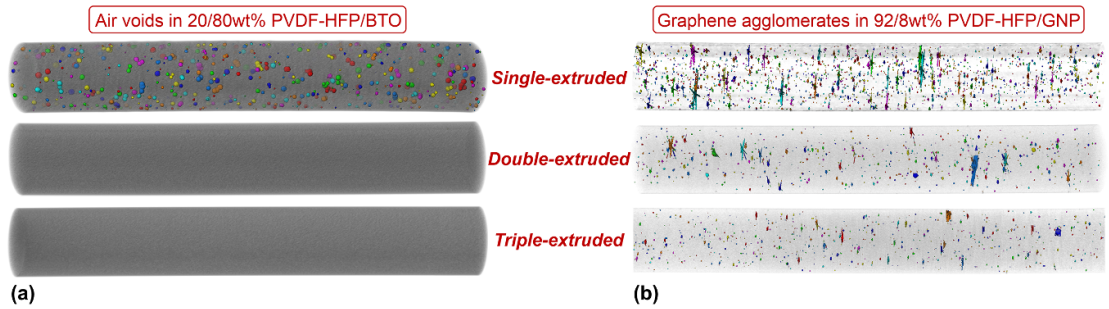

Figure 4. 3D visualization of (a) air void distribution in PVDF-HFP/BTO filaments and (b) graphene agglomerate distribution in PVDF-HFP/GNP filaments after single-, double- and triple-extrusion process.

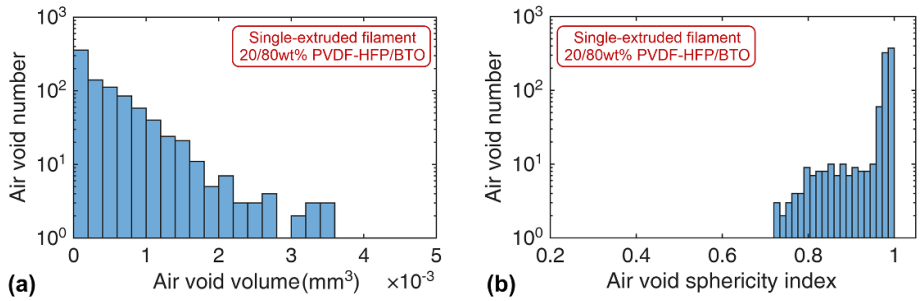

Figure 5. Histograms of (a) volume and (b) sphericity index of voids for single-extruded PVDF-HFP/BTO filament (F1-BTO80).

2.7. Physicochemical characterizations

Surface morphology of composites was examined with SEM Phenom ProX (Thermo Fisher Scientific, USA) operated at 10 kV. The samples were sputtered with a thin gold layer using a coater Q150R (Quorum Technologies, UK). Characteristic FTIR peaks of PVDF-HFP phases were recorded in 650–4000 cm^{-1} with 2 cm^{-1} resolution using Spectrum Two spectrometer with a UATR diamond accessory (PerkinElmer, USA). The electroactive β-phase fraction in PVDF-HFP was evaluated using the Beer–Lambert law:

$$F_\beta = \frac{A_{840}}{(K_\beta/K_\alpha)A_{762} + A_{840}} \times 100\% \quad (1)$$

where A_{762} and A_{840} are the absorbance intensities of the α- and β-phase bands at 762 cm^{-1} and 840 cm^{-1}, respectively; K_α and K_β are the respective standard absorption coefficients of 6.1×10^4 and 7.7×10^4 cm^2mol^{-1} [66].

3. Results and discussion

3.1. Micro-CT defectoscopy

The micro-CT data (figure 4(a)) indicates that the pockets with entrapped air (voids) are present in the single-extruded piezocomposite filament F1-BTO80 (e.g. ∼900 air voids with total volume of 0.44 mm^3 in a sample of ∼10 mm length). The majority of the voids are spherical and smaller than ∼0.001 mm^3 (figure 5). We note that the re-extrusion process provides both homogenizing and degassing effects since air void content is negligible in the re-extruded piezocomposites (figure 4(a)).

Micro-CT imaging does not reveal BTO agglomerates, which suggests that the particles are relatively uniformly dispersed in the matrix (it is also visible in the SEM images in section 3.3). However, we note that agglomerates smaller than 9 voxels (∼3.4×10^{-6} mm^3) were filtered out and may still be present. Such particle clusters are relatively small when considering that the average BTO particle size is ∼0.5 μm.

Contrary to the highly filled piezocomposite (80 wt% BTO), air voids are not detected in the conductive composite filaments, where filler weight fraction is an order of magnitude smaller (8 wt% GNP). However, GNP agglomerates are clearly visible, and the single-extruded filament exhibits substantial

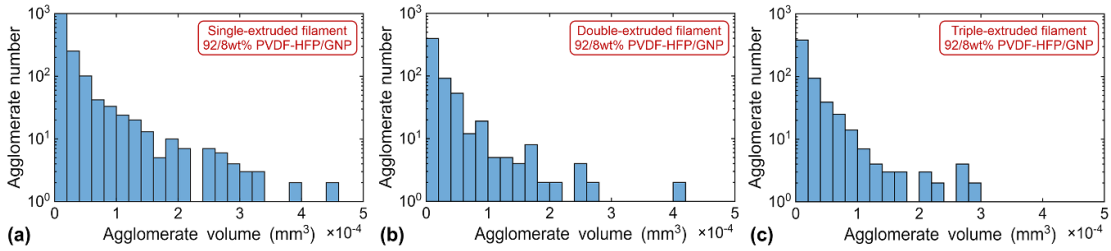

Figure 6. Histograms of GNP agglomerate volume for the single-, double- and triple-extruded PVDF-HFP/GNP filaments: (a) F1-GNP8, (b) F2-GNP8, (c) F3-GNP8.

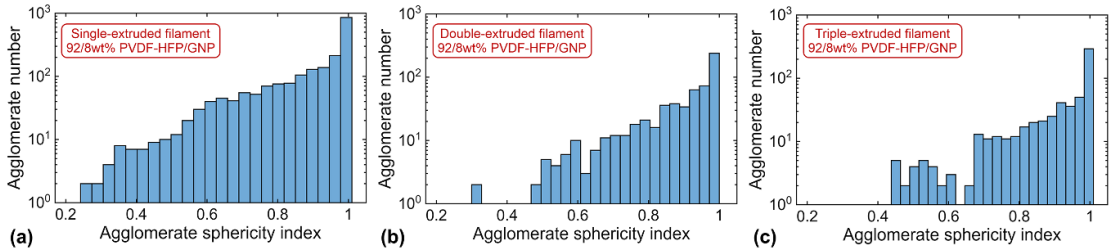

Figure 7. Histograms of GNP agglomerate sphericity index (Wadell's true sphericity index S_w) for the single-, double- and triple-extruded PVDF-HFP/GNP filaments: (a) F1-GNP8, (b) F2-GNP8, (c) F3-GNP8.

agglomeration with numerous elongated clusters (figure 4(b)). The re-extrusion proves to be an effective deagglomeration process, which significantly reduces the number and size of GNP clusters (most are below ∼0.0002 mm^3 as shown in figures 6(b) and (c)). Moreover, it also promotes agglomerate spheroidization as evident from the lower content of strongly irregular ($S_w \lesssim 0.5$–0.6) clusters in the re-extruded filaments (figure 7). Nevertheless, many GNP agglomerates retain a relatively irregular shape ($S_w \approx 0.6$–0.9) even after three extrusions. Overall, the similarity in agglomerate morphology between the F2-GNP8 and F3-GNP8 samples (figures 6 and 7) indicates that the third extrusion step provides only a minor additional reduction in agglomeration beyond the major improvement achieved by the second extrusion.

3.2. Phase composition of melt-processed PVDF-HFP

The FTIR spectra reveal distinct phase-specific vibrational bands of PVDF-HFP (figure S3) that are influenced by melt-processing conditions and composite structure (filler type and content). The phase-specific peak intensities in the prints are lower than in the filaments. Assignment of widely reported characteristic peaks is presented in figure S3 and is based on [66, 67].

Figure 8 indicates that the electroactive β-phase fractions are noticeably higher in the piezocomposite filaments ($F_\beta \approx 83$–98%) than in the prints ($F_\beta \approx 42\%$–45%). The increase in F_β is typically associated with the combined influence of processing-specific thermal history and shear forces [19], which differ substantially between filament extrusion and FFF processes. During filament extrusion, the composites are processed at a significantly lower temperature (∼170 °C–180 °C) than during FFF (260 °C). Similar lower-temperature melt processing was previously reported to increase F_β compared to a higher-temperature regime (>200 °C) [13, 48]. However, we emphasize that the combined temperature-shear effect on PVDF crystallization is complex since some studies show that even ∼10 °C–20 °C change in melt processing temperature can appreciably modify F_β depending on shear rate [19]. In contrast, no increase in F_β is observed for the conductive composite filaments or prints. Overall, this suggests an intricate interrelationship between filler type, its content and melt processing conditions in modulating electroactive phase formation in PVDF. In addition, electrical poling was found to slightly increase F_β from ∼45% to ∼57%, which was also observed in our earlier study [48] and is commonly attributed to partial phase transformation and dipole realignment [7, 67].

Finally, we note that XRD analysis was performed in our previous study on the lower-filled PVDF-HFP/BTO composites and confirmed the presence of ferroelectric tetragonal structure within Inframat BTO [48]. Thus, as the BTO particles are polarizable, the applied poling regime was found to affect the electrical properties of the piezocomposite (section 3.4).

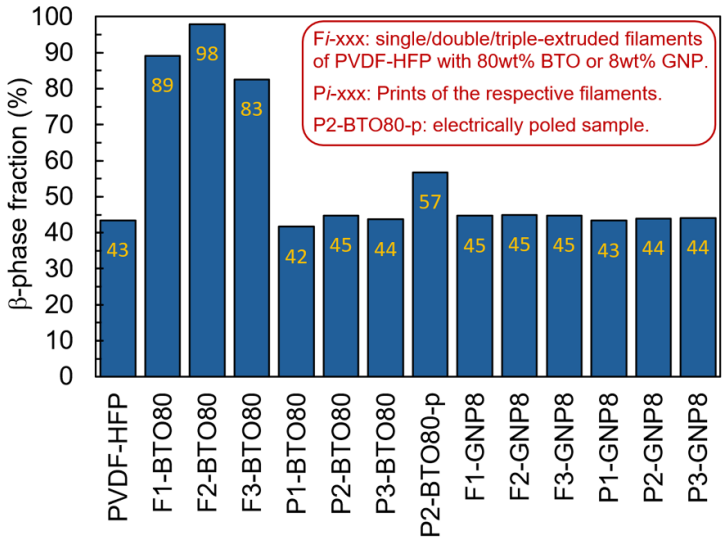

Figure 8. Estimated electroactive β-phase fraction in single-, double- and triple-extruded 20/80 wt% PVDF-HFP/BTO filaments (F*i*-BTO80) and prints (P*i*-BTO80) including poled one (P2-BTO80-p), 92/8 wt% PVDF-HFP/GNP filaments (F*i*-GNP8) and prints (P*i*-GNP8), including Kynar 2501–20 powder (PVDF-HFP).

3.3. Mechanical properties

The re-extrusion process modifies the distribution of fillers and micro-defects in the composites (section 3.1). Moreover, despite superior thermal stability of PVDF [48], repeated remelting during filament fabrication and printing may cause slight structural degradation of the polymer matrix. Therefore, it is necessary to determine how the applied melt-based workflow affects mechanical properties of neat (P*i*-BTO80) and electroded (P–ES) piezocomposites.

Under quasi-static tension the piezocomposites exhibit predominantly brittle behavior without plastic yielding before rupture, which occurs along a clean and nearly planar fracture path (figure 9(a)). This material behavior is expected because plastic deformation in highly filled composites is heavily suppressed [68], including PVDF-HFP composites with hard fillers [69–71]. The brittle failure mode of the piezocomposite is demonstrated by the fracture surface microtexture (figure 10), which lacks plastic deformation features (e.g. elongated fibrils due to stretching of highly ductile PVDF-HFP [48, 69]). Instead, surface morphology appears relatively similar at different strain rates (microtexture tends to be more uniform at 1000 mm min^{-1}). The surface presents irregular, rough and cleavage-like stepped microtexture with lamellar-type formations in the piezocomposite, where the closely packed BTO particles are clearly visible (figures 10(a) and (b)). Similar morphology was also observed in other ceramic-rich composites [68], including PVDF-HFP with 60 wt% BTO [48]. Meanwhile, the fracture behavior of the conductive PVDF-HFP/GNP composite exhibits more pronounced strain rate dependence (figures 10(c) and (d)). The highly textured and deeply ridged surface morphology at 10 mm min^{-1} indicates a transitional semi-ductile failure mode, which is characterized by moderate plastic flow and the absence of the fibrillation typical of highly ductile fracture [48, 69]. In contrast, at 1000 mm min^{-1}, the conductive composite undergoes mostly brittle fracture. It produces uniformly rough and step-like surface microtexture without plastic deformation features (it is similar to piezocomposite microtexture at lower SEM magnification in figure 10(d)).

The stiffness of the piezocomposite is higher by nearly an order of magnitude compared to neat PVDF-HFP (tensile modulus of ∼3.2–3.3 GPa vs 0.35 GPa [72]). Nevertheless, we note that the highly ductile Kynar Superflex® matrix imparts acceptable flexibility to the composites (figure 2(a), figure 9(a)). When loaded at 10–1000 mm min^{-1}, the fracture strains of P3-BTO80 and P–ES samples reach ∼1.6–3.8%, which aligns with reported values for other PVDF-HFP composites with similar filler content ($\gtrsim$50 wt%) [70, 71]. It indicates that during tensile testing the PVDF-HFP was not loaded until its yield point (∼18% for Kynar Superflex® [72]). This order-of-magnitude reduction in fracture strain (vs >50% for PVDF-HFP [72]) is consistent with reports for other highly filled particulate composites [68].

The inferior mechanical properties of P1-BTO80 samples show that the first extrusion produces under-homogenized composite (figures 9(b) and (c)). In contrast, P2-BTO80 demonstrates improved mechanical properties, which indicates that the second extrusion step noticeably enhances BTO dispersion homogeneity. The third extrusion appears to provide a moderate additional homogenizing

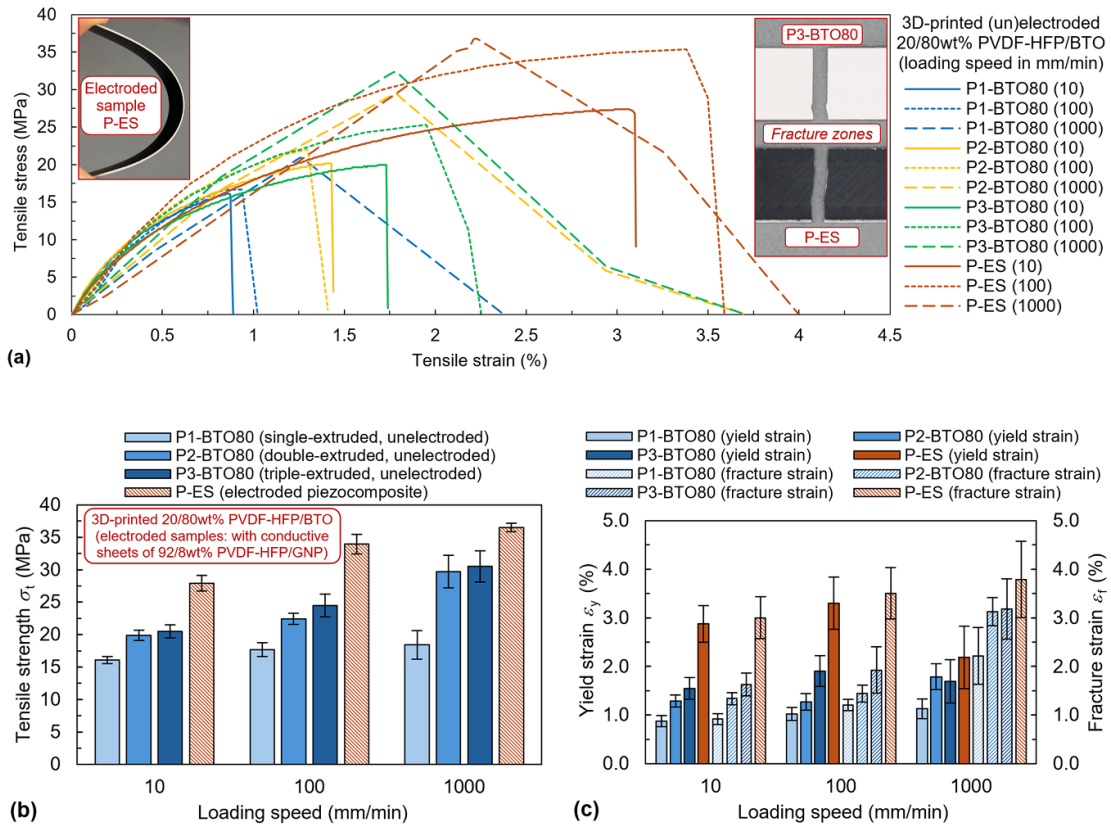

Figure 9. (a) Tensile stress–strain curves and (b)–(c) mechanical properties (at different loading speeds) of 20/80 wt% PVDF-HFP/BTO piezocomposites P*i*-BTO80 (3D-printed with single-, double- and triple-extruded filaments), and piezocomposites P–ES electroded with 92/8 wt% PVDF-HFP/GNP sheets (3D-printed with triple-extruded filaments).

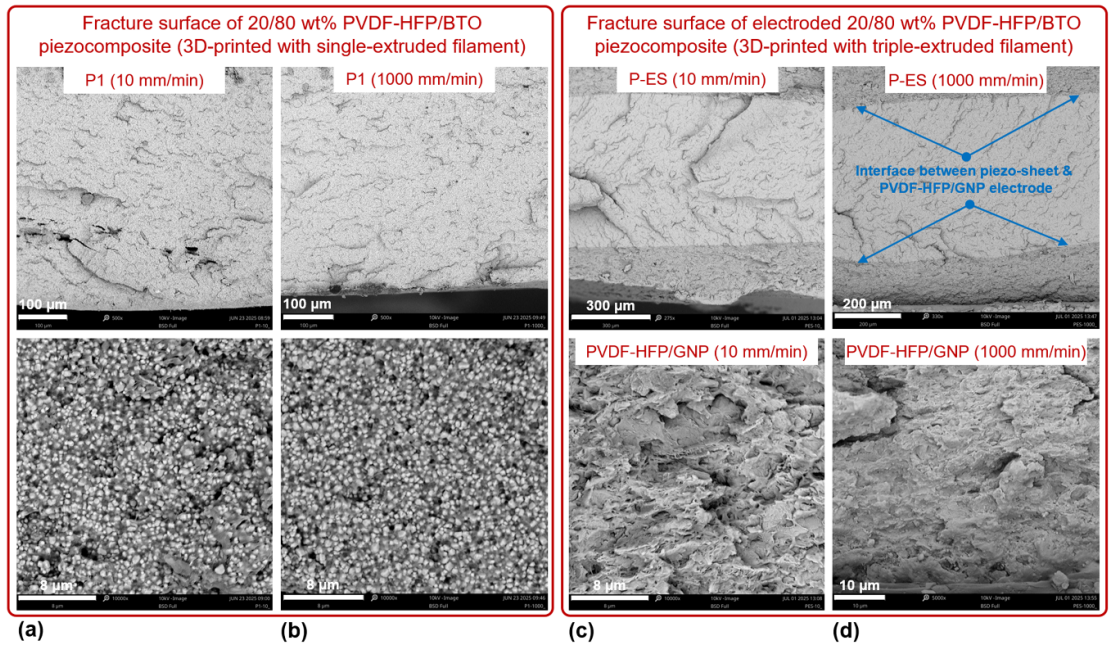

Figure 10. SEM fractographs of 3D-printed tensile thin strips of triple-extruded piezocomposites loaded at different speeds: (a)–(b) unelectroded samples, (c)–(d) samples electroded with 92/8 wt% PVDF-HFP/GNP sheets.

effect since properties of P2-BTO80 and P3-BTO80 are comparable. The re-extruded samples also exhibit strain-rate strengthening effect that is characteristic to high-quality composites [73] (the effect is insignificant for the under-homogenized P1-BTO80). The strength of P2-BTO80 and P3-BTO80 samples is increased by ∼50% from ∼20 MPa at 10 mm min^{-1} to ∼30 MPa at 1000 mm min^{-1}. Moreover,

a slight improvement in piezocomposite ductility is observed after each extrusion cycle (figure 9(c)), including the strain-rate softening effect (P3-BTO80 fracture strain increases from 1.63 to 3.18% at 10 and 1000 mm min^{-1}, respectively). The electroded P–ES samples also exhibit strain rate dependence with improving strength and ductility (strength increases by ∼31% up to ∼37 MPa in the 10–1000 mm min^{-1} range).

Overall, micro-CT and tensile test results demonstrate that the double- and triple-extrusion workflow produces effectively homogenized electroactive filaments, which enable printing well-fused composite samples. Favorable mechanical properties without noticeable BTO pullout (figures 10(b) and (c)) suggest that the interfacial debonding is not significant and the filler–matrix adhesion is sufficient to prevent BTO separation from the matrix. This is a noteworthy outcome because BTO-PVDF surface compatibility is generally considered to be relatively low [74]. The poor interfacial affinity arises from the substantial mismatch between the low surface energy of hydrophobic PVDF and the very high surface energy of hydrophilic BTO (assuming the untreated ceramic surface is hydroxylated [57]). We note that interfacial debonding was also not observed in another study on composites containing well-dispersed untreated BTO particles [52]. This supports the conclusion that the re-extrusion/granulation workflow is an effective filler homogenization process. The well-dispersed BTO state appears to partially compensate for the intrinsically poor interfacial affinity. Moreover, several reports [52, 75] suggest that optimization of filler dispersion may be a more critical determinant of composite performance than chemical filler–matrix compatibilization. Filler surface functionalization with coupling agents is widely applied [74] to enhance filler dispersibility and interfacial bonding [57]. However, there is a risk that these benefits may be offset by losses in the electrical properties of ferroelectric composites [52].

Even though the improvement in mechanical properties after the third extrusion cycle was limited, achieving the maximum microstructural quality of the printed composites is critical to minimize the defect-dependent likelihood of dielectric breakdown when targeting the highest possible poling fields and peak piezoelectric performance (section 3.4.3). The third extrusion cycle provides additional shear mixing that further reduces filler agglomerates (section 3.1) and homogenizes dispersion, which is a key determinant of composite performance [57]. Furthermore, the better-dispersed filler state facilitates consistent printing [58] of more uniformly fused layers, likely reducing micro-defects (air voids) as indicated by the slightly better mechanical properties of the triple-extruded samples (figure 9). Because micro-defects significantly affect poling efficiency [59], the printed triple-extruded piezocomposites were less prone to breakdown under strong poling fields ($\gtrsim$20 kV mm^{-1}). Preliminary experiments revealed that the maximum achievable fields for double-extruded samples were lower by up to ∼0.5 kV mm^{-1}. We consider this moderately improved dielectric strength of the triple-extruded samples to be crucial for mitigating breakdown risk and reducing the failed sample count during extensive poling experiments aimed at reaching the upper polarizability threshold to maximize the induced piezoresponse. Nonetheless, it should be noted that the double-extrusion workflow remains a viable, effective alternative for similar composites utilizing polymers with thermal reprocessing capabilities inferior to those of exceptionally resilient PVDF.

3.4. Electrical properties

3.4.1. Dielectric properties

Figure 11 presents the frequency-dependent dielectric properties of the printed and poled single-track piezocomposites. The dielectric constant ε' at 10^3 Hz reaches 108 and 103 for the samples poled at 20 and 40 kV mm^{-1}, respectively (table 3). These values are within the upper permittivity range commonly reported for highly filled lead-free composites (table 4), and reach the level of the solvent-processed counterpart ($\varepsilon' \approx 107$ for 60 vol% untreated Inframat BTO [53]).

The measured ε' values are generally consistent with the effective-medium predictions applicable for biphasic 0–3 composites (equations (2)–(4) for the Jayasundere–Smith, Maxwell–Garnett and Bruggeman models, respectively [76]):

$$\varepsilon_{\text{eff}}^{\text{J-S}} = \frac{\varepsilon_{\text{m}}(1-V_{\text{f}}) + \varepsilon_{\text{f}}V_{\text{f}}[3\varepsilon_{\text{m}}/(\varepsilon_{\text{f}}+2\varepsilon_{\text{m}})]\,[1+3V_{\text{f}}(\varepsilon_{\text{f}}-\varepsilon_{\text{m}})/(\varepsilon_{\text{f}}+2\varepsilon_{\text{m}})]}{(1-V_{\text{f}}) + V_{\text{f}}(3\varepsilon_{\text{m}})/(\varepsilon_{\text{f}}+2\varepsilon_{\text{m}})\,[1+3V_{\text{f}}(\varepsilon_{\text{f}}-\varepsilon_{\text{m}})/(\varepsilon_{\text{f}}+2\varepsilon_{\text{m}})]} \tag{2}$$

$$\varepsilon_{\text{eff}}^{\text{M-G}} = \varepsilon_{\text{m}}\left[1 + \frac{3V_{\text{f}}(\varepsilon_{\text{f}}-\varepsilon_{\text{m}})}{(1-V_{\text{f}})(\varepsilon_{\text{f}}-\varepsilon_{\text{m}}) + 3\varepsilon_{\text{m}}}\right] \tag{3}$$

$$\frac{\varepsilon_{\text{f}}-\varepsilon_{\text{eff}}}{\varepsilon_{\text{eff}}^{1/3}} = \frac{(1-V_{\text{f}})(\varepsilon_{\text{f}}-\varepsilon_{\text{m}})}{\varepsilon_{\text{m}}^{1/3}} \tag{4}$$

where V_{f}—filler volume fraction, ε_{f}, ε_{m}—dielectric constants of filler and matrix materials, respectively.

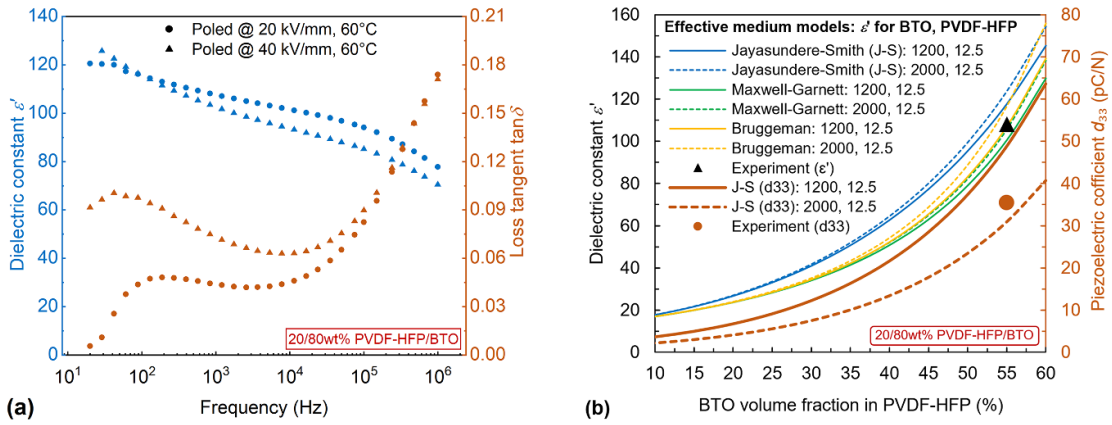

Figure 11. (a) Dielectric constant and loss tangent as a function of frequency for FFF-printed silver-coated single-track samples (∼15 × 2 × 0.1 mm^3) of triple-extruded PVDF-HFP/BTO piezocomposites poled at 60 °C under DC fields of 20 kV mm^{-1} and 40 kV mm^{-1}. (b) Maximum ε' and d_{33} values measured in this study for the poled samples, compared with predictions of well-known effective medium models [76, 77].

Table 3. Summary of material properties of FFF-printed 20/80 wt% PVDF-HFP/BTO piezocomposite.

Property	Values
σ_t (MPa)	20.5 ± 0.97 (@ 0.003 s^{-1}), 24.5 ± 1.75 (@ 0.033 s^{-1}), 30.5 ± 2.37 (@ 0.33 s^{-1})
ε_f (%)	1.63 ± 0.23 (@ 0.003 s^{-1}), 1.93 ± 0.48 (@ 0.033 s^{-1}), 3.18 ± 0.62 (@ 0.33 s^{-1})
E_t (GPa)	3.2 ± 0.13
ε' (RT, 1 kHz)	108 (poled @ 20 kV mm^{-1}), 103 (poled @ 40 kV mm^{-1})
tanδ (RT, 1 kHz)	0.044 (poled @ 20 kV mm^{-1}), 0.073 (poled @ 40 kV mm^{-1})
ε' (RT, 1 MHz)	78 (poled @ 20 kV mm^{-1}), 70 (poled @ 40 kV mm^{-1})
tanδ (RT, 1 MHz)	0.174 (poled @ 20 kV mm^{-1}), 0.171 (poled @ 40 kV mm^{-1})
P_r (μC cm^{-2})	2.78 (10 Hz; poled @ 20 kV mm^{-1}), 3.98 (10 Hz; poled @ 40 kV mm^{-1})
P_{max} (μC cm^{-2})	3.89 (10 Hz; poled @ 20 kV mm^{-1}), 6.77 (10 Hz; poled @ 40 kV mm^{-1})
E_c (kV mm^{-1})	18.5 (10 Hz; poled @ 20 kV mm^{-1}), 14.5 (10 Hz; poled @ 40 kV mm^{-1})
d_{33} (pC N^{-1})	35.4 ± 0.32 (neat piezocomposite), 30.3 ± 0.28 (with co-printed electrodes)

Table 4. Comparison of representative highly filled PVDF-based composites (≳50 vol% lead-free ferroelectric particles).

Material composition	Processing	ε'	d_{33} (pC N^{-1})	References
PVDF-TrFE/BTO 40/60 vol%	Solvent-free (molding)	∼92	∼3 (−33 @ 20 vol% BTO)	[54]
PVDF-TrFE/BTO 40/60 vol%	Solvent-based (casting)	∼85	—	[52]
PVDF-TrFE/BTO 40/60 vol%	Solvent-based (molding)	∼107	∼7–10	[53]
PVDF-HFP/BTO 50/50 vol%	Solvent-based (spin coating)	57	—	[50]
PVDF-HFP/BTO 45/55 vol%	Solvent-based (molding)	∼103	—	[51]
PVDF/BTO 25/75 wt%	Solvent-based (FFF)	∼37	—	[49]
PVDF-TrFE/BTO 45/55 vol%	Solvent-based (screen printing)	∼130	∼7	[78]
PVDF/KNN 20/80 wt%	Solvent-based (molding)	∼113	∼23	[55]
PVDF-HFP/BTO 45/55 vol%	Solvent-free (FFF)	108	35.4	**This work**

Figure 11(b) shows that the Jayasundere–Smith model predicts slightly larger ε' values compared to the Maxwell–Garnett and Bruggeman counterparts that match the measured ε' values more closely.

The measured spectra (figure 11) show a typical [79–83] frequency-dependent gradual ε' reduction for the piezocomposites poled at weaker (20 kV mm^{-1}) and stronger (40 kV mm^{-1}) DC fields. We note that even the 20 kV mm^{-1} field was able to induce appreciable ferroelectric polarization in BTO filler as demonstrated by relatively high piezoresponses (section 3.4.3). The increase of dielectric constant and losses in the low-frequency range at ∼10^1–10^2 Hz are commonly explained by additional contribution of space charges [52, 79, 82, 84, 85], i.e. by Maxwell–Wagner–Sillars (MWS) interfacial polarization effect [86]. It is expected to be substantial due to high BTO content that entails a large interfacial area at filler–matrix (interphase) boundaries [52, 53, 82]. MWS polarization effect manifests as the relaxation of space charges trapped at interphase boundaries due to mismatch in conductivity (σ_f, σ_m) and permittivity (ε_f, ε_m) of the phases [86]. A necessary condition for the MWS polarization is a mismatch of

Maxwell charge-relaxation times $\tau = \varepsilon\varepsilon_0/\sigma$, i.e. $\tau_m \neq \tau_f$ or $\varepsilon_m/\sigma_m \neq \varepsilon_f/\sigma_f$ [87]. In our case, the mismatch $\tau_m/\tau_f = (\varepsilon_m\sigma_f)/(\varepsilon_f\sigma_m)$ is expected to be significant as it may reach at least one or two orders of magnitude when considering the RT values of $\sigma_m \approx 5 \times 10^{-15}$ S cm^{-1} [72], $\varepsilon_m \approx 12.5$ (at 1 kHz Hz) [88] for PVDF-HFP, and $\sigma_f \approx 10^{-11}$–$10^{-10}$ S cm^{-1} [89], $\varepsilon_f \approx 1200$–$2000$ [90] for BTO.

The ε' values for the stronger-field poling case (40 kV mm^{-1}) are slightly smaller than for 20 kV mm^{-1} within $\sim 10^3$–10^6 Hz range, where the contribution of interfacial polarization is minimal [85, 91]. A part of this difference in ε' may arise from dimensional variations (e.g. layer thickness). However, it is also plausible [53] that doubling the poling field E_{app} from 20 to 40 kV mm^{-1} produces a modest but measurable permittivity-reducing effect on the closely packed BTO particles (figure 10(a)). In the highly filled piezocomposite, the interparticle distance d_i is expected to be smaller relative to average particle radius r_p ($d_i \ll r_p$), which increases the effective electrical field (internal DC bias) E_{eff} within the particles according to $E_{eff} = ((1 + r_p/d_i)\varepsilon_m/(\varepsilon_f + (r_p/d_i)\varepsilon_m))E_{app}$ [58]. In BTO ceramics studies, a stronger DC bias is known to reduce the out-of-plane permittivity (along poling direction) [92, 93]. The BTO domain state is stabilized at a stronger bias, which may reduce extrinsic domain-wall contribution to the permittivity [94]. Thus, the slightly lower ε' after 40 kV mm^{-1} poling is consistent with the increased E_{eff}, which also aligns with the enhanced ferroelectric responses for the stronger-field poling case (section 3.4.2). Overall, the reduced dielectric constant is advantageous for piezoelectric sensing performance that scales as d_{33}/ε' [94], but comes at the expense of higher dielectric losses (table 3).

The measured spectra (figure 11) reveal an increase of dielectric losses in the low-frequency range at $\sim 10^1$–10^2 Hz, minimization at $\sim 10^4$–10^5 Hz and subsequent increase towards 10^6 Hz. Similar frequency-dependent evolution of loss tangent was observed in other PVDF composites [53, 80, 82, 83, 95]. The measured low-frequency tanδ peaks are consistent with the MWS relaxation phenomenon as supported by prior studies on highly filled composites with 30–60 vol% of untreated Inframat BTO particles [52]. Moreover, it was widely reported that at low frequencies the dielectric constant and losses were noticeably reduced when surface-treated fillers were used [52, 82]. It suggests that filler–matrix interfacial effects are dominant and are closely linked to the suppression of low-frequency dielectric losses compared to the untreated filler case [52]. These findings suggest appreciable contribution of MWS polarization to tanδ increase at $\sim 10^1$–10^2 Hz. Nevertheless, the collective impact of other polarization and leakage mechanisms cannot be excluded in the densely packed piezocomposite (figure 10(a)), which is a more complex heterogeneous material in terms of filler–matrix connectivity. Theoretically, an idealized 0–3 configuration is geometrically possible near ~50 vol% for non-interacting spheres [96]. However, in practice the piezocomposite configuration is nonhomogeneous due to the likely formation of highly interconnected particle clusters throughout the sample. In such a quasi-percolating filler state the closely packed particles form (semi) continuous connected filler networks [57, 97, 98]. They facilitate charge migration by acting as partially conducting pathways due to $\sigma_f \gg \sigma_m$ and induce leakage currents at low frequencies f_e (DC conduction losses $\tan\delta_{cond} \approx \sigma_{DC}/2\pi f_e\varepsilon_0\varepsilon'$) [80, 99]. In addition, it is known that the semi-crystalline PVDF-HFP copolymer itself is a heterogeneous material with crystalline and amorphous regions that differ in conductivity and permittivity (i.e. local MWS relaxation may be observed [88]). Finally, it may be noted that dielectric spectral features associated with dipolar relaxation in a polymer matrix may be distorted by interfacial effects including MWS and electrode polarization phenomena [91, 100].

The dielectric spectra reveal that in the low-frequency range the tanδ peak is significantly larger for the stronger-field poling case compared to the weaker-field case. It is noted that in the $\sim 10^1$–10^2 Hz range, the ε' values for both poling cases are similar, and even slightly larger after 40 kV mm^{-1} poling, which is contrary to the behavior at higher frequencies. The difference in dielectric losses between the two poling cases progressively decreases at higher frequencies, where tanδ increases in the $\sim 10^4$–10^5 Hz range until the values converge at $\sim 10^5$–10^6 Hz (i.e. molecular/dipolar polarization regime [79]). Overall, the results indicate a significant contribution of poling-modulated interfacial polarization at lower frequencies, which is sensitive to poling history through changes in the density of trapped interfacial charges [53]. It suggests that stronger-field poling at 40 kV mm^{-1} can enhance more significantly the interfacial charge trapping compared to 20 kV mm^{-1} poling case. As a result, higher space charge density may increase the low-frequency dielectric constant together with leakage and dielectric loss [53, 85].

3.4.2. Ferroelectric responses

Polarization and displacement hysteresis loops were measured for the printed silver-coated single-track piezocomposites to confirm ferroelectric response and examine dependence on poling history (figure 12).

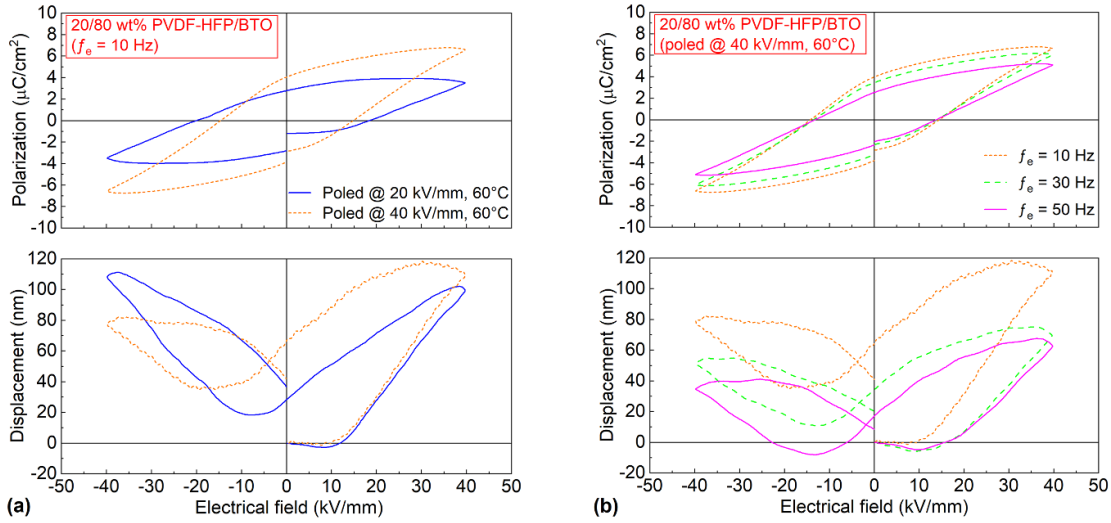

Figure 12. *P–E* and *D–E* hysteresis loops for FFF-printed silver-coated single-track samples (∼15 × 2 × 0.1 mm^3) of triple-extruded PVDF-HFP/BTO piezocomposites: (a) poled at 60 °C under DC fields E_{ext} of 20 kV mm^{-1} and 40 kV mm^{-1} (measured at 10 Hz), (b) poled at 60 °C under 40 kV mm^{-1} (measured at 10, 30 and 50 Hz).

The measurements reveal leaky *P–E* loops with non-saturated polarization hysteresis and moderate remanent polarization P_r (table 3), which is typical for the piezocomposites [44, 77, 82, 101]. Such loops represent a combination of lossy dielectric (non-switching) response and ferroelectric switching response [102]. The latter is primarily governed by the domain switching in BTO particles since electrical field up to 40 kV mm^{-1} cannot induce appreciable ferroelectric response in PVDF-HFP [48] (very high coercive field of $\gtrsim$70 kV mm^{-1} [103]).

Typically, well-saturated ferroelectric ceramics produce vertical square-like *P–E* loops when the switching is complete, although coarse-grained BTO can exhibit slightly tilted (slanted) loops [102]. The leaky *P–E* loops of the piezocomposite are ellipse-like and highly tilted, which suggests combined influence of two mechanisms. First, the dielectric loss mechanisms, including MWS polarization and conductive contributions, introduce a phase lag between the polarization and electric field that manifests as ellipse-like *P–E* loop that is characteristic of a lossy capacitive response [102]. Due to relatively large filler–matrix interfacial area and the expected quasi-percolating connectivity at ∼55 vol% BTO [97, 104], it is plausible that these losses are influenced by the interfacial charge accumulation and leakage processes [77, 82] (section 3.4.1). Second, the minimal squareness and lack of polarization saturation are consistent with incomplete domain switching in BTO particles, which is typical for piezocomposites and is caused by the local-field screening effect since $\varepsilon_m \ll \varepsilon_f$. The internal field E_{eff} acting on BTO particles is substantially reduced relative to the applied field [58] ($E_{eff} \approx (3\varepsilon_m/\varepsilon_f)E_{app}$ when $\varepsilon_m \ll \varepsilon_f$ based on Maxwell–Garnett theory [105]). Thus, despite the intrinsically low coercive field of BTO (typically $E_c \lesssim 1$ kV mm^{-1} [106]), significant filler–matrix permittivity mismatch strongly limits the achievable degree of ferroelectric polarization. We note that DC poling history has a noticeable influence on ferroelectric hysteresis (figure 12(a)). Doubling of poling field strength from 20 to 40 kV mm^{-1} produces less tilted *P–E* loops with more noticeable squareness, approaching towards the shape of the coarse-grained BTO ceramics [102], and increasing P_r and P_{max} by 43% and 74%, respectively (table 3). This indicates improved BTO domain switching since a stronger DC field promotes formation and retention of a larger portion of stabilized domains, which can be more effectively realigned during post-poling AC excitation [94]. The enhanced ferroelectric switching after stronger-field poling is also evident from the stronger nonlinear electromechanical response observed in the *D–E* loops for the 40 kV mm^{-1} case (figure 12(a)).

Frequency increase from 10 to 50 Hz (figure 12(b)) produces slightly more tilted and slimmer *P–E* loops, reducing P_r and P_{max} by ∼36% and ∼23%, respectively (table 3). More pronounced loop tilting with increasing frequency follows the general trend [102] and was earlier observed for other highly filled piezocomposites [77]. This suggests that the measured polarization includes a substantial ferroelectric switching component since P_r and P_{max} typically tend to decrease at higher frequencies, where BTO domains have less time to realign. It is further supported by the smaller displacement amplitudes at 50 Hz compared to 10 Hz (figure 12(b)), which indicates reduced strain associated with limited ferroelectric switching at shorter AC excitation timescales. However, it is likely that interfacial charges

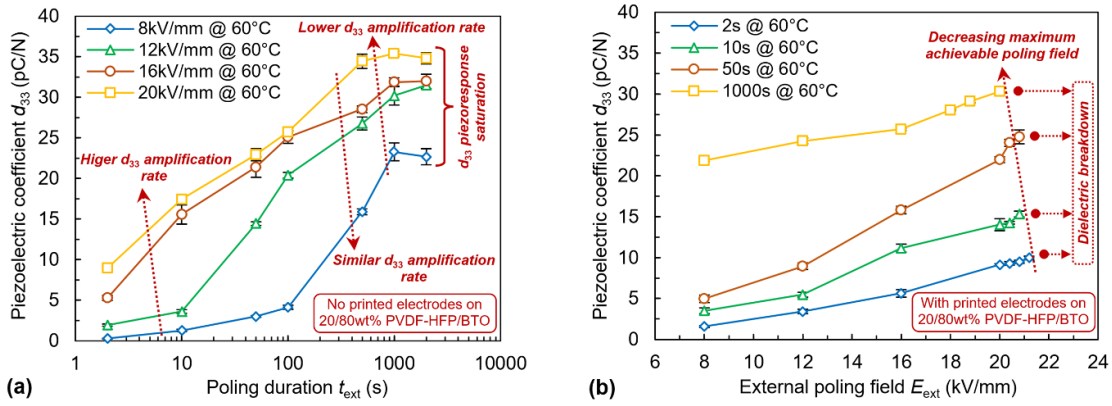

Figure 13. Longitudinal piezoresponse of the printed sheets (10 × 10 × 0.5 mm^3) of triple-extruded PVDF-HFP/BTO composite as a function of: (a) contact poling duration at different external poling fields applied at 60 °C (copper foil electrodes), (b) external poling field increased until maximum breakdown-free level using different poling durations (sheets with co-printed and ironed 92/8 wt% PVDF-HFP/GNP electrodes).

also contribute to the measured polarization in the densely packed piezocomposite (section 3.4.1). The broader *P*–*E* loops of larger area at lower frequencies refer to increased energy dissipation, which pertains to higher leakage losses [77] and, possibly, the contribution of interfacial polarization [82]. In summary, the measured hysteresis loops confirm a sufficiently strong ferroelectric response, which is likely enabled by the highly continuous (quasi-percolating) filler connectivity [97, 104]. This in turn translates into an appreciable macroscopic d_{33} piezoresponse.

3.4.3. Piezoelectric responses

Figure 13 present d_{33} measurements for neat and electroded triple-extruded piezocomposites (with co-printed electrodes), poled in contact mode using DC fields of $E_{ext} \approx$ 8–21 kV mm^{-1} for durations of $t_{ext} \approx$ 2–2000 s. The conductivity of the triple-extruded filaments with 2, 4 and 8 wt% GNP was determined as 0.0042 ± 0.0005, 0.28 ± 0.04 and 1.59 ± 0.07 S cm^{-1}, respectively. These values suggest that the percolation threshold is slightly below 2 wt% GNP, which is consistent with prior composites percolating below 3 wt% graphene content [62]. The achieved maximum conductivity of ∼1.6 S cm^{-1} falls within the upper range reported for solvent-cast and melt-processed graphene composites [62] and represents a three-fold increase over the solvent-based counterpart [63]. Therefore, the mechanically compliant 92/8 wt% PVDF-HFP/GNP filament was selected for co-printing of sensor electrodes. Parallel and perpendicular sheet resistance of the ironed electrodes (∼0.12 mm thickness) were 84.4 ± 7.17 and 94.2 ± 6.51 Ω/sq, respectively, enabling effective contact poling.

The piezoelectric characterizations were divided into two stages. Initially, a wider experimental study was performed on the neat piezocomposites, where a larger set of t_{ext} values was tested with fields up to 20 kV mm^{-1}. The objective was to establish field- and duration-dependent d_{33} amplification trends (figure 13(a)), which served as a basis for a more focused parametric study using the piezocomposites co-printed with the ironed electrodes (figure 13(b)). It is noted that a transient d_{33} decay was observed in all the samples during the initial ∼1–2 d after poling (figure S4) as discussed in SI. The d_{33} values recorded after ∼56 h on the polarization-stabilized piezocomposites were used for further analysis (figure 13).

The piezoresponses are amplified with larger poling field and duration until the maximum d_{33} is achieved after poling for ∼1000 s (figure 13(a)). It corresponds to a duration-saturated piezoresponse state since longer poling for $\gtrsim$1000 s has minimal impact on d_{33} level. The duration-dependent d_{33} amplification rate (slope $\Delta d_{33}/\Delta t_{ext}$) evolves differently with increasing E_{ext}. $\Delta d_{33}/\Delta t_{ext}$ shows strong field dependence in the short-duration range of ∼2–10 s as poling at higher fields of 16–20 kV mm^{-1} results in more pronounced d_{33} amplification compared to 8–12 kV mm^{-1} range. It is noted that short poling for 10 s at 16–20 kV mm^{-1} can produce appreciable piezoresponses of ∼15–17 pC N^{-1}. In the intermediate regime of ∼100–500 s, the d_{33} strongly depends on the t_{ext} and the amplification rate $\Delta d_{33}/\Delta t_{ext}$ equalizes over the entire 8–20 kV mm^{-1} range. In the long-duration regime of ∼500–1000 s, the $\Delta d_{33}/\Delta t_{ext}$ shows field dependence that is opposite to the ∼2–10 s duration case. Piezocomposite poling at a relatively weak field of 8 kV mm^{-1} produces significant d_{33} amplification, while the influence of $\gtrsim$12 kV mm^{-1} fields is moderate. At 20 kV mm^{-1}, the d_{33} is similar over the ∼500–2000 s range, which indicates that noticeably shorter poling can maximize piezoresponse when sufficiently strong field

is applied. It implies that this strong-field regime induces duration-saturated polarization in the BTO particles, which delivers the maximum d_{33} recorded in this study (35.4 ± 0.32 pC N^{-1}). It generally agrees with predictions of the Jayasundere–Smith model (figure 11(b)) [77]:

$$d_{33}^{J-S} = \left(1 + \frac{3V_f\varepsilon_f}{2\varepsilon_m + \varepsilon_f}\right)\frac{\varepsilon_{eff}^{J-S}}{\varepsilon_f} d_{33,f}. \quad (5)$$

We note that the ∼35.4 pC N^{-1} piezoresponse is nearly 5-fold higher than we achieved earlier for the lower-filled piezocomposite with ∼31 vol% BTO [48]. It suggests that filler connectivity (quasi-percolating state) is substantially enhanced within ∼30–55 vol% BTO range, which likely leads to significantly larger field concentration (E_{eff}) in the filler [97, 104]. In addition, the E_{eff} level is also increased due to the thermally assisted poling regime (60 °C). It is more efficient than room-temperature poling [48] as it reduces filler–matrix conductivity mismatch (i.e. ratio σ_m/σ_f shifts closer to one) [107]. It was reported that PVDF-HFP conductivity σ_m increases substantially at elevated temperatures (possibly by ∼2–3 orders of magnitude at 60 °C [88]). In contrast, the corresponding increase in BTO conductivity σ_f is likely modest (possibly less than an order of magnitude [89]). Consequently, σ_m approaches σ_f when poling at the elevated temperature, which is expected to increase E_{eff} due to its strong dependence on the ratio σ_m/σ_f [107]. It is considered that poling efficiency is predominantly governed by this ratio when t_{ext} is larger than the characteristic interfacial relaxation time (estimated to be in the sub-second range according to $\tau_{MW} \approx (\varepsilon_m\varepsilon_0 + \varepsilon_f\varepsilon_0)/(\sigma_m + \sigma_f)$ [87]).

Next, a smaller set of t_{ext} values was selected to evaluate the field-dependent d_{33} amplification for the electroded piezocomposite (i.e. basic piezoelectric sensor). The objective was to produce the largest possible d_{33} when poling with the maximum achievable breakdown-free field (figure 13(b)). First, we note that the ultra-short poling for several seconds can produce a practically usable piezoresponse of ∼10 pC N^{-1} at 21.2 kV mm^{-1}. This is the highest E_{ext} level that the printed sheets could sustain during poling experiments. In comparison, the single-track samples exhibit even better breakdown strength (up to ∼40 kV mm^{-1}) as there are no fusion zones with intra- and inter-laminar defects that highly elevate the likelihood of breakdown. In the case of short-duration poling for ∼10–50 s, the adequate piezoresponses of $\gtrsim$5–10 pC N^{-1} are generated by using at least ∼12–16 kV mm^{-1} (i.e. poling fields that are more than an order of magnitude larger than $E_c \lesssim 1$ kV mm^{-1} of BTO [106]). The sub-minute poling for 50 s using strong fields of $\gtrsim$20.4 kV mm^{-1} produces markedly higher piezoresponses of ∼24–25 pC N^{-1}. Meanwhile, the 20-fold increase of t_{ext} from 50 to 1000 s has only a modest amplification effect since the maximum d_{33} peaks at ∼30.3 pC N^{-1}. The breakdown threshold drops slightly with prolonged poling as the maximum achievable field decreases from ∼21 to ∼20 kV mm^{-1} when comparing the short- and long-duration poling regimes (figure 13(b)).

Overall, we note that the piezoresponse attenuation is moderate when the manually bonded copper foil electrodes are replaced with the printed GNP-doped composite electrodes (∼35.4 → ∼30.3 pC/N). These d_{33} values are higher than those reported for highly filled lead-free analogues including the solvent-processed non-printed (molded, cast) PVDF-based composites (table 4). Meanwhile, FFF-printed PVDF homopolymer typically produces $\lesssim$10 pC/N (table 5), and higher d_{33} up to 18 pC/N was reported for the costlier PVDF-TrFE [108]. The d_{33} of FFF-printed lead-free 0–3 piezocomposites hardly exceeds ∼20 pC/N (table 5), while values up to 28 pC/N were reported for the solvent-processed composite [31]. Unfortunately, many studies on FFF-printed piezocomposites with ferroelectric fillers do not include d_{33} measurements (table S1), while the ferroelectric characterizations are even less common. Furthermore, the reported piezoresponse studies are frequently limited to small (E_{ext}, t_{ext}) ranges, which in turn impedes more rigorous cross-study benchmarking of the piezoelectric performance under diverse poling regimes.

In addition, the sensor-level electromechanical performance was characterized under flexural resonant excitation of the host cantilever, which was bonded with two piezocomposite sensor samples printed using identical FFF settings and poled at 20 kV mm^{-1} (figures 14(a) and S2). The sensors under bending demonstrate excellent d_{31}-mode voltage output linearity ($R^2 > 0.995$) and repeatability, with maximum coefficient of variation below 4.5% and 2.1% for samples A and B, respectively (figure 14(b)). The voltage sensitivity was derived from the slope of the linear regression line fitting the average V_{rms} values across the 0.25–3.5 g excitation range. Samples A and B exhibit comparable sensitivities of 21.68 and 20.17 mV g^{-1}, respectively, indicating high reproducibility of the implemented multi-material FFF workflow.

Table 5. Comparison of representative FFF-printed PVDF-based piezopolymers and 0–3 lead-free piezocomposites.

Material composition	Processing	Printed electrodes	ε'	d_{33} (pC/N)	References
PVDF	Solvent-free	No	—	0.05	[11]
PVDF	Solvent-free	No	—	1.85	[14]
PVDF	Solvent-free	No	—	5	[16]
PVDF	Solvent-free	No	—	7.29	[17]
PVDF-TrFE	Solvent-free	No	—	9.97	[18]
PVDF-TrFE	Solvent-free	No	—	18	[108]
PVDF	Solvent-free	Yes	—	0.72	[22]
PVDF/BTO 60/40 wt%	Solvent-based	No	∼19	28	[31]
PVDF/KNN 65/35 vol%	Solvent-based	No	—	12.1	[36]
PVDF/BTO 85/15 wt%	Solvent-based	No	—	0.1	[28]
PVDF/KNN	Solvent-based	No	—	4.2	[30]
PVDF-HFP/KNN 65/35 vol%	Solvent-based	Yes	∼69.1	16.1	[24]
PVDF/BTO 80/20 wt%	Solvent-free	No	—	20	[42]
PVDF/BTO 70/30 wt%	Solvent-free	No	∼15	4.2	[44]
PVDF-HFP/BTO 45/55 vol%	Solvent-free	No	108	35.4	**This work**
PVDF-HFP/BTO 45/55 vol%	Solvent-free	Yes	—	30.3	**This work**

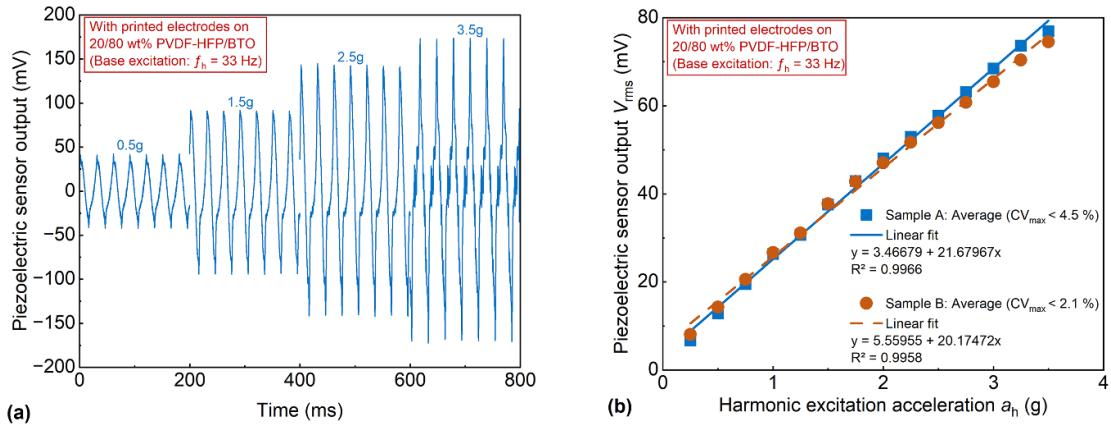

Figure 14. Bending-mode sensing performance of the 3D-printed piezocomposite sensors (40 × 13.5 × 0.72 mm^3) on a host cantilever under flexural resonant excitation (33 Hz): (a) representative voltage signals recorded via transimpedance amplifier (1 mV nA^{-1}) at different accelerations, (b) average RMS output ($n = 3$) vs. acceleration for two sensor samples mounted side by side on the cantilever (error bars are omitted as they are smaller than the data markers).

4. Conclusions

Electroactive filaments of well-mixed highly filled 20/80 wt% PVDF-HFP/BTO piezocomposite and conductive composite with 2, 4 and 8 wt% GNPs were fabricated through a scalable and sustainable solvent-free re-extrusion/granulation process. The double- and triple-extrusion process eliminated air voids in the ceramic-rich piezocomposite and provided increasingly homogeneous filler dispersion in the graphene-doped composite. A fine-tuned FFF workflow delivered uniform deposition of relatively viscous melts to enable clogging-free printing of well-fused composite layers to form piezoelectric sensors. The printed re-extruded composites demonstrated favorable mechanical and electrical characteristics. Strain-rate strengthening of up to ∼50% was observed when the loading speed increased by two orders of magnitude. Comparable mechanical properties of the printed double- and triple-extruded samples indicate that double extrusion could be sufficient for successful fabrication of well-performing composites utilizing less resilient polymers that might not sustain multiple re-extrusions without thermal degradation.

The filament with 8 wt% GNP achieved satisfactory flexibility and conductivity of ∼1.6 S cm^{-1} sufficient for effective poling with co-printed electrodes (sheet resistance <100 Ω/sq). The printed re-extruded piezocomposite provided sufficient breakdown strength to withstand thermal poling up to 20–40 kV mm^{-1} at 60 °C, producing relatively strong ferroelectric and piezoelectric responses. This indicates effective ferroelectric polarization of closely packed BTO particles, which is possibly facilitated by quasi-percolating connectivity that is likely at ∼55 vol% ceramic content. Due to numerous interphase boundaries, the observed lossy ferroelectric responses, partial post-poling depolarization and increased

low-frequency dielectric properties may be attributed to poling-modulated interfacial charge contributions. The measured maximum values of d_{33} (~35.4 pC N^{-1}) and dielectric constant (up to ~108 at 1 kHz) are consistent with effective-medium predictions. The achieved maximum d_{33} represents a performance level not commonly observed in FFF-printed piezoelectric materials and exceeds d_{33} of highly filled lead-free PVDF composites produced via solvent-assisted non-additive processes. The 3D-printed sensors mounted on a vibrating host cantilever demonstrated practically usable d_{31}-mode sensitivity with high linearity and repeatability. Moreover, the sensors generated ~24–25 pC N^{-1} after sub-minute poling at ~20 kV mm^{-1}, suggesting that the composites may be suitable for rapid printer-integrated poling to enable monolithic embedding of piezoelectric components into co-printed structures. Overall, the cost-efficient solvent-free fabrication workflow presented here serves as a readily accessible route for pursuing on-demand MEX AM of customized sensing and energy-harvesting devices.

Acknowledgmentss

This project has received funding from the Research Council of Lithuania (LMTLT), Agreement No. S-MIP-24-39. The corresponding author gratefully acknowledges Dr Martynas Sborikas (aixACCT Systems GmbH) for his support with the ferroelectric and piezoelectric characterizations.

Data availability statement

All data that support the findings of this study are included within the article (and any supplementary files).

Conflict of interest

The authors declare that there is no conflict of interest.

Ethical approval

This study does not contain any studies with human or animal subjects performed by any of the authors.

Author contributions

Gopi Kompelli 0000-0002-6674-0728
Conceptualization (equal), Data curation (lead), Formal analysis (equal), Investigation (lead), Methodology (equal), Validation (equal), Visualization (equal), Writing – original draft (lead)

Rolanas Dauksevicius 0000-0002-4571-757X
Conceptualization (equal), Formal analysis (equal), Funding acquisition (lead), Investigation (equal), Methodology (equal), Resources (equal), Supervision (lead), Validation (equal), Visualization (equal), Writing – review & editing (lead)

Šarūnas Svirskas 0000-0003-1271-8063
Data curation (supporting), Formal analysis (supporting), Investigation (equal), Methodology (equal), Resources (equal), Validation (supporting), Visualization (supporting), Writing – review & editing (supporting)

Elena Jasiūnienė 0000-0002-8073-5597
Data curation (supporting), Formal analysis (supporting), Investigation (equal), Methodology (equal), Resources (equal), Validation (supporting), Visualization (supporting), Writing – review & editing (supporting)

Vaidotas Cicenas 0000-0001-5475-3874
Data curation (supporting), Formal analysis (supporting), Investigation (supporting), Methodology (supporting), Visualization (supporting)

Roman Turczyn 0000-0001-6221-634X
Data curation (supporting), Investigation (equal), Methodology (equal), Resources (equal), Visualization (supporting)

References

[1] Yuan X, Mai Z, Li Z, Yu Z, Ci P and Dong S 2023 A 3D-printing approach toward flexible piezoelectronics with function diversity *Mater. Today* **69** 160–92
[2] Megdich A, Habibi M and Laperrière L 2025 Review of progress in 4D printing of piezoelectric energy harvesters *Mater. Sci. Eng. R* **166** 101072
[3] Selicani G V, Mobin M, Esposito V, Insinga A R and Haugen A B 2025 Shape engineering and manufacturing of piezoceramics for energy conversion—a review *J. Phys. Energy* **7** 022004
[4] Li S, Shan Y, Chen J, Chen X, Shi Z, Zhao L, He R and Li Y 2024 3D printing and biomedical applications of piezoelectric composites: a critical review *Adv. Mater. Technol.* **9** 2401160
[5] Wolstrup A F, Spangenberg J, Yamamoto A, Gleadall A and Zsurzsan G 2025 Advances in 3D printed electromechanical sensors: performance comparison, trends, and future directions *Addit. Manuf.* **106** 104799
[6] Koroglu L, Ayas E and Ay N 2021 3D printing of polyvinylidene fluoride based piezoelectric nanocomposites: an overview *Macromol. Mater. Eng.* **306** 2100277
[7] Costa C M *et al* 2023 Smart and multifunctional materials based on electroactive poly(vinylidene fluoride): recent advances and opportunities in sensors, actuators, energy, environmental, and biomedical applications *Chem. Rev.* **123** 11392–487
[8] Lee C and Tarbutton J A 2014 Electric poling-assisted additive manufacturing process for PVDF polymer-based piezoelectric device applications *Smart Mater. Struct.* **23** 095044
[9] Bhandari S, Vajpayee G, da Silva L L, Hinterstein M, Franchin G and Colombo P 2025 A review on additive manufacturing of piezoelectric ceramics: from feedstock development to properties of sintered parts *Mater. Sci. Eng. R* **162** 100877
[10] Goh G D, Wong K K, Tan N, Seet H L and Nai M L S 2024 Large-format additive manufacturing of polymers: a review of fabrication processes, materials, and design *Virtual Phys. Prototyp.* **19** e2336160
[11] Kim H, Torres F, Wu Y, Villagran D, Lin Y and Tseng T-L 2017 Integrated 3D printing and corona poling process of PVDF piezoelectric films for pressure sensor application *Smart Mater. Struct.* **26** 085027
[12] Burnham-fay E D, Le T, Tarbutton J A and Ellis J D 2017 Strain characteristics of additive manufactured polyvinylidene fluoride (PVDF) actuators *Sensors Actuators A* **266** 85–92
[13] Porter D A *et al* 2017 Effects of *in-situ* poling and process parameters on fused filament fabrication printed PVDF sheet mechanical and electrical properties *Addit. Manuf.* **13** 81–92
[14] Pei H, Xie Y, Xiong Y, Lv Q and Chen Y 2021 A novel polarization-free 3D printing strategy for fabrication of poly (Vinylidene fluoride) based nanocomposite piezoelectric energy harvester *Compos. B* **225** 109312
[15] Lee C and Tarbutton J A 2019 Polyvinylidene fluoride (PVDF) direct printing for sensors and actuators *Int. J. Adv. Manuf. Technol.* **104** 3155–62
[16] Dinesh Kumar A, Arunachalam N and Jayaganthan R 2024 Effect of poling methods on the functional properties of fused deposition modeling printed polyvinylidene fluoride for sensing application *J. Mater. Eng. Perform* **34** 1695-704
[17] Tao R, Shi J, Rafiee M, Akbarzadeh A and Therriault D 2022 Fused filament fabrication of PVDF films for piezoelectric sensing and energy harvesting applications *Mater. Adv.* **3** 4851–60
[18] Islam S, Cheheltani S, Cheng C and Fowler V M *2024* 3D-Printable self-powered piezoelectric smart stent for wireless endoleaks sensing *2024 IEEE 37th Int. Conf. on Micro Electro Mechanical Systems (MEMS) (IEEE)* pp 789–92
[19] Lannunziata E, Fiorillo C, Minetola P, Edeleva M, Cardon L and Iuliano L 2025 Study of flow-induced crystallization in polyvinylidene fluoride 3D printing *Int. J. Adv. Manuf. Technol.* **137** 117–29
[20] Košir T and Slavič J 2023 Manufacturing of single-process 3D-printed piezoelectric sensors with electromagnetic protection using thermoplastic material extrusion *Addit. Manuf.* **73** 103688
[21] Zhang H, Ke F, Shao J, Wang C, Wang H and Chen Y 2022 One-step fabrication of highly sensitive pressure sensor by all FDM printing *Compos. Sci. Technol.* **226** 109531
[22] Košir T and Slavič J 2022 Single-process fused filament fabrication 3D-printed high-sensitivity dynamic piezoelectric sensor *Addit. Manuf.* **49** 102482
[23] Pei H, Chen Y, Lv Q, Peng Z, Wang X, Chen N and Zhang H 2024 A novel microwave assisted multi-material 3D printing strategy to architect lamellar piezoelectric generators for intelligent sensing *Compos. B* **280** 111529
[24] Li J, Yang F, Long Y, Dong Y, Wang Y and Wang X 2021 Bulk ferroelectric metamaterial with enhanced piezoelectric and biomimetic mechanical properties from additive manufacturing *ACS Nano* **15** 14903–14
[25] Tao R, Shi J, Granier F, Moeini M, Akbarzadeh A and Therriault D 2022 Multi-material fused filament fabrication of flexible 3D piezoelectric nanocomposite lattices for pressure sensing and energy harvesting applications *Appl. Mater. Today* **29**
[26] Fan J, Deneke N, Xu S, Newell B, Garcia J, Davis C, Wu W, Voyles R M and Nawrocki R A 2022 Electric poling-assisted additive manufacturing technique for piezoelectric active poly(vinylidene fluoride) films: towards fully three-dimensional printed functional materials *Addit. Manuf.* **60**
[27] Rafiee M, Granier F, Tao R, Bhérer-constant A, Chenier G and Therriault D 2022 Multi-material, multi-process, planar, and nonplanar additive manufacturing of piezoelectric devices *Adv. Eng. Mater.* **24** 2200294
[28] Kim H, Torres F, Villagran D, Stewart C, Lin Y and Tseng T B 2017 3D Printing of BaTiO 3 /PVDF composites with electric *in situ* poling for pressure sensor applications *Macromol. Mater. Eng.* **302** 2200294
[29] Liu X, Shang Y, Liu J, Shao Z and Zhang C 2022 3D printing-enabled *in-situ* orientation of BaTi 2 O 5 nanorods in β-PVDF for high-efficiency piezoelectric energy harvesters *ACS Appl. Mater. Interfaces* **14** 13361–8
[30] Pan F, Sui J, Silva-pedraza Z, Bontekoe J, Carlos C R, Wu G, Liu W, Gao J, Liu B and Wang X 2024 3D-Printed piezoelectric stents for electricity generation driven by pressure fluctuation *ACS Appl. Mater. Interfaces* **16** 27705–13
[31] Megdich A, Habibi M, Laperrière L, Li Z and Abdin Y 2024 Advanced 3D-printed PVDF/BT piezoelectric energy harvester with a bio-inspired 3D structure for a self-powered smart mouse *Nano Energy* **128** 109876
[32] Kim H, Fernando T, Li M, Lin Y and Tseng T-L B 2018 Fabrication and characterization of 3D printed BaTiO 3 /PVDF nanocomposites *J. Compos. Mater.* **52** 197–206

[33] Sharma R, Singh R, Batish A and Ranjan N 2023 On mechanical, thermal, morphological, and 4D capabilities of polyvinylidene fluoride nanocomposites: effect of mechanical and chemical-assisted mechanical blending *J. Mater. Eng. Perform* **32** 1938–53
[34] Kim H, Wilburn B R, Castro E, Garcia Rosales C A, Chavez L A, Tseng T-L B and Lin Y 2019 Multifunctional SENSING using 3D printed CNTs/BaTiO 3 /PVDF nanocomposites *J. Compos. Mater.* **53** 1319–28
[35] Kim H, Islam M T, Md Didarul I, Chavez L A, Garcia Rosales C A, Wilburn B R, Stewart C M, Noveron J C, Tseng T-L B and Lin Y 2017 Increased piezoelectric response in functional nanocomposites through multiwall carbon nanotube interface and fused-deposition modeling three-dimensional printing *MRS Commun.* **7** 960–6
[36] Li J *et al* 2020 Multifunctional artificial artery from direct 3D printing with built-in ferroelectricity and tissue-matching modulus for real-time sensing and occlusion monitoring *Adv. Funct. Mater.* **30** 2002868
[37] Prat D, Wells A, Hayler J, Sneddon H, McElroy C R, Abou-shehada S and Dunn P J 2016 CHEM21 selection guide of classical- and less classical-solvents *Green Chem.* **18** 288–96
[38] ECHA- European Chemicals Agency Registered substances factsheets. Substance Infocard (N,N-dimethylformamide), REACH-registration, evaluation, authorisation and restriction of chemicals (available at: https://echa.europa.eu/substance-information/-/substanceinfo/100.000.617))
[39] Lopez A *et al* 2025 Additive manufacturing of hybrid polymer–ceramic anisotropic 3D structures for directional piezoelectric sensing *Smart Mater. Struct.* **34** 095015
[40] Pejak S D and Sola A 2022 Emerging research in conductive materials for fused filament fabrication: a critical review *Adv. Eng. Mater.* **24** 2101476
[41] Qi X, Huang X, Das B, Dong M, Restasari A, Whiteley R, Yan H, Bilotti E and Reece M J 2024 Processing and characterisation of hot rolling pressed PVDF films with enhanced field-induced polarisation *Polymer* **302** 127001
[42] Sharma R, Singh R and Batish A 2021 Study on barium titanate and graphene reinforced PVDF matrix for 4D applications *J. Thermoplast. Compos. Mater.* **34** 1234–53
[43] Simunec D P, Porcincula D H, Ford M J, Kolibaba T J, Fein-ashley B, Brodsky J, Killgore J P and Sellinger A 2023 Electrical capability of 3D printed unpoled polyvinylidene fluoride (PVDF)/thermoplastic polyurethane (TPU) sensors combined with carbon black and barium titanate *Addit. Manuf.* **73**
[44] Pei H, Shi S, Chen Y, Xiong Y and Lv Q 2022 Combining solid-state shear milling and FFF 3D-Printing strategy to fabricate high-performance biomimetic wearable fish-scale PVDF-based piezoelectric energy harvesters *ACS Appl. Mater. Interfaces* **14** 15346–59
[45] Sebastian T, Bach M, Geiger A, Lusiola T, Kozielski L and Clemens F 2021 Investigation of electromechanical properties on 3-D printed piezoelectric composite scaffold structures *Materials* **14** 5927
[46] Acosta M, Novak N, Rojas V, Patel S, Vaish R, Koruza J, Rossetti G A and Rödel J 2017 BaTiO3-based piezoelectrics: fundamentals, current status, and perspectives *Appl. Phys. Rev.* **4**
[47] Joshi S, Gazmin E, Glover J, Weeks N, Khan F, Iacono S and Corti G 2022 Improved electrical signal of non-poled 3D printed zinc oxide-polyvinylidene fluoride nanocomposites *Polymers* **14** 4312
[48] Kompelli G, Dauksevicius R, Kleiva A, Turczyn R and Krukiewicz K 2025 3D printable piezoelectric composites manufactured via scalable and sustainable solvent-free multi-extrusion process *Smart Mater. Struct.* **34** 025028
[49] Kim H, Johnson J, Chavez L A, Garcia Rosales C A, Tseng T-L B and Lin Y 2018 Enhanced dielectric properties of three phase dielectric MWCNTs/BaTiO3/PVDF nanocomposites for energy storage using fused deposition modeling 3D printing *Ceram. Int.* **44** 9037–44
[50] Ehrhardt C, Fettkenhauer C, Glenneberg J, Münchgesang W, Leipner H S, Wagner G, Diestelhorst M, Pientschke C, Beige H and Ebbinghaus S G 2014 Enhanced dielectric properties of sol–gel-BaTiO 3 /P(VDF-HFP) composite films without surface functionalization *RSC Adv.* **4** 40321–9
[51] Fu J, Hou Y, Zheng M, Wei Q, Zhu M and Yan H 2015 Improving dielectric properties OF PVDF composites by employing surface modified strong polarized BaTiO 3 particles derived by molten salt method *ACS Appl. Mater. Interfaces* **7** 24480–91
[52] Dalle Vacche S, Michaud V, Damjanovic D, Månson J-A E and Leterrier Y 2018 Improved mechanical dispersion or use of coupling agents? Advantages and disadvantages for the properties of fluoropolymer/ceramic composites *Polymer* **154** 8–16
[53] Dalle Vacche S, Leterrier Y, Michaud V, Damjanovic D, Aebersold A B and Månson J-A E 2015 Effect of interfacial interactions on the electromechanical response of poly(vinylidene fluoride-trifluoroethylene)/BaTiO3 composites and its time dependence after poling *Compos. Sci. Technol.* **114** 103–9
[54] Otero A, Sayagués M J, Romero F J, Gotor F J and Moriche R 2025 Piezoelectric and dielectric response of BaTiO 3 /PVDF-TrFE composites with high β-phase content *ACS Appl. Polym. Mater.* **7** 7848–58
[55] Mirzazadeh Z, Sherafat Z and Bagherzadeh E 2021 Physical and mechanical properties of PVDF/KNN composite produced via hot compression molding *Ceram. Int.* **47** 6211–9
[56] Brettmann B K, Kalman J, McCollum J M, Moore L M J, Savage A M and McClain M S 2025 Challenges and opportunities in manufacturing highly filled polymers *npj Adv. Manuf.* **2** 34
[57] Rueda M M, Auscher M-C, Fulchiron R, Périé T, Martin G, Sonntag P and Cassagnau P 2017 Rheology and applications of highly filled polymers: a review of current understanding *Prog. Polym. Sci.* **66** 22–53
[58] Eltouby P, Shyha I, Li C and Khaliq J 2021 Factors affecting the piezoelectric performance of ceramic-polymer composites: a comprehensive review *Ceram. Int.* **47** 17813–25
[59] Dani S S, Tripathy A, Alluri N R, Balasubramaniam S and Ramadoss A 2022 A critical review: the impact of electrical poling on the longitudinal piezoelectric strain coefficient *Mater. Adv.* **3** 8886–921
[60] Gonzalez-gutierrez J, Cano S, Schuschnigg S, Kukla C, Sapkota J and Holzer C 2018 Additive manufacturing of metallic and ceramic components by the material extrusion of highly-filled polymers: a review and future perspectives *Materials* **11** 840
[61] Chen B, Feng Z, Yao F-Z, Zhang M-H, Wang K, Wei Y, Gong W and Rödel J 2025 Flexible piezoelectrics: integration of sensing, actuating and energy harvesting *npj Flex. Electron.* **9** 58
[62] Lalire T, Longuet C and Taguet A 2024 Electrical properties of graphene/multiphase polymer nanocomposites: a review *Carbon N. Y.* **225** 119055
[63] Díaz-mena V, Sánchez-romate X F, Sánchez M and Ureña A 2025 Graphene nanoplatelets—PVDF stretchable sensors for tactile interaction: from grasp detection to Morse code communication *Polym. Compos.* **46** 17379–91
[64] Cruz-matías I, Ayala D, Hiller D, Gutsch S, Zacharias M, Estradé S and Peiró F 2019 Sphericity and roundness computation for particles using the extreme vertices model *J. Comput. Sci.* **30** 28–40
[65] Fei W, Narsilio G A and Disfani M M 2019 Impact of three-dimensional sphericity and roundness on heat transfer in granular materials *Powder Technol.* **355** 770–81

[66] Cai X, Lei T, Sun D and Lin L 2017 A critical analysis of the α, β and γ phases in poly(vinylidene fluoride) using FTIR *RSC Adv.* **7** 15382–9
[67] Martins P, Lopes A C and Lanceros-mendez S 2014 Electroactive phases of poly(vinylidene fluoride): determination, processing and applications *Prog. Polym. Sci.* **39** 683–706
[68] Wolff M F H, Salikov V, Antonyuk S, Heinrich S and Schneider G A 2014 Novel, highly-filled ceramic–polymer composites synthesized by a spouted bed spray granulation process *Compos. Sci. Technol.* **90** 154–9
[69] Mullaveettil F N, Dauksevicius R, Rimasauskas M and Grigaliunas V 2021 Fused filament fabrication and mechanical performance of PVDF-based specialty thermoplastics *Int. J. Adv. Manuf. Technol.* **117** 3267–80
[70] Yuennan J, Nateethorn C, Samakphong P, Siri R, Tohluebaji N, Ashraf G A, Khanklaeo A and Channuie P 2025 Structural and shielding properties of P(VDF-HFP)-Bi2O3 multilayered polymer composites *J. Sci. Adv. Mater. Devices* **10**
[71] Du Q, Shi S, Zhang L, Yan Z, Zeng X, Wu J, Zhou W, Huang Z, Masese T and Ma Y 2022 Silica Nanowires Reinforced with Poly(vinylidene fluoride-co-hexafluoropropylene): separator for high-performance lithium batteries *ChemNanoMat* **8**
[72] Arkema Inc. Brochure: Kynar Fluoropolymers—Performance Characteristics & Data 2017 (available at: https://hpp.arkema.com/en/product-families/kynar-fluoropolymer-family/contact-physical-and-mechanical-properties/)
[73] Kim M, Park T Y and Hong S 2021 Experimental determination of the plastic deformation and fracture behavior of polypropylene composites under various strain rates *Polym. Test.* **93** 107010
[74] Bouad V, Girardot M, Ladmiral V and Barrau S 2024 Piezoelectric fluorinated polymer composites: a review on coupling agents at the filler/matrix interface *Polym. Compos.* **45** 3861–82
[75] Iyer K A and Torkelson J M 2015 Importance of superior dispersion versus filler surface modification in producing robust polymer nanocomposites: the example of polypropylene/nanosilica hybrids *Polymer* **68** 147–57
[76] Wu H, Zhuo F, Qiao H, Kodumudi Venkataraman L, Zheng M, Wang S, Huang H, Li B, Mao X and Zhang Q 2022 Polymer-/ceramic-based dielectric composites for energy storage and conversion *ENERGY Environ. Mater.* **5** 486–514
[77] Stuber V L *et al* 2020 The effect of the intrinsic electrical matrix conductivity on the piezoelectric charge constant of piezoelectric composites *Mater. Res. Express* **7** 015703
[78] Revenant C, Minot S, Toinet S, Lawrence Bright E, Ramos R and Benwadih M 2024 Spatially-resolved *in-situ*/operando structural study of screen-printed BaTiO3/P(VDF-TrFE) flexible piezoelectric device *Sensors Actuators A* **377** 115738
[79] Hao Y N, Bi K, O'brien S, Wang X X, Lombardi J, Pearsall F, Li W L, Lei M, Wu Y and Li L T 2017 Interface structure, precursor rheology and dielectric properties of BaTiO 3 /PVDF–HFP nanocomposite films prepared from colloidal perovskite nanoparticles *RSC Adv.* **7** 32886–92
[80] Huang E-Q, Zhao J, Zha J-W, Zhang L, Liao R-J and Dang Z-M 2014 Preparation and wide-frequency dielectric properties of (Ba0.5Sr0.4Ca0.1)TiO3/poly(vinylidene fluoride) composites *J. Appl. Phys.* **115** 194102
[81] Song S, Li Y, Wang Q and Zhang C 2021 Facile preparation of high loading filled PVDF/BaTiO 3 piezoelectric composites for selective laser sintering 3D printing *RSC Adv.* **11** 37923–31
[82] Lu H, Lin J, Yang W and Liu L 2017 Improved dielectric strength and loss tangent by interface modification in PI@BCZT/PVDF nano-composite films with high permittivity *J. Mater. Sci., Mater. Electron.* **28** 13360–70
[83] Shuzeng H, Ye L, Ran C, Yan T, Li H and Zhang J 2024 Dielectric and energy storage properties of BaTiO3/PVDF composite films fabricated by a spin-coating process *Polym. Sci. Ser. A* **66** 253–61
[84] Ait Laasri H, Fasquelle D, Tachafine A, Carru J-C, Rguiti M and Elaatmani M 2021 Ferroelectric BT–PVDF composite thick films for electrical energy storage *J. Electron. Mater.* **50** 1132–9
[85] Shen Z-H, Wang J-J, Zhang X, Lin Y, Nan C-W, Chen L-Q and Shen Y 2017 Space charge effects on the dielectric response of polymer nanocomposites *Appl. Phys. Lett.* **111**
[86] Steeman P A M and van Turnhout J 2003 *Dielectric Properties of Inhomogeneous Media Broadband Dielectric Spectroscopy* (Springer Berlin Heidelberg) pp 495–522
[87] Prodromakis T and Papavassiliou C 2009 Engineering the Maxwell–Wagner polarization effect *Appl. Surf. Sci.* **255** 6989–94
[88] Kochervinskii V V, Malyshkina I A, Markin G V, Gavrilova N D and Bessonova N P 2007 Dielectric relaxation in vinylidene fluoride–hexafluoropropylene copolymers *J. Appl. Polym. Sci.* **105** 1101–17
[89] Tyunina M 2021 Conductivity in ferroelectric barium titanate: electrons versus oxygen vacancies *IEEE Trans. Ultrason. Ferroelectr. Freq. Control* **68** 296–302
[90] Renteria A, Diaz J A, He B, Renteria-marquez I A, Chavez L A, Regis J E, Liu Y, Espalin D, Tseng T-L (Bill) and Lin Y 2019 Particle size influence on material properties of BaTiO 3 ceramics fabricated using freeze-form extrusion 3D printing *Mater. Res. Express* **6** 115211
[91] Samet M, Kallel A and Serghei A 2022 Maxwell-Wagner-Sillars interfacial polarization in dielectric spectra of composite materials: scaling laws and applications *J. Compos. Mater.* **56** 3197–217
[92] Yoon S-H, Kim M-Y and Kim D 2020 Correlation between tetragonality (c/a) and direct current (DC) bias characteristics of BaTiO 3 -based multi-layer ceramic capacitors (MLCC) *J. Mater. Chem. C* **8** 9373–81
[93] Misra S, Kalaswad M, Zhang D and Wang H 2020 Dynamic tuning of dielectric permittivity in BaTiO 3 via electrical biasing *Mater. Res. Lett.* **8** 321–7
[94] Fujii I and Trolier-mckinstry S 2023 Temperature dependence of dielectric nonlinearity of $BaTiO_3$ ceramics *Microstructures* **3**
[95] Belovickis J, Ivanov M, Svirskas Š, Samulionis V, Banys J, Solnyshkin A V, Gavrilov S A, Nekludov K N, Shvartsman V V and Silibin M V 2018 Dielectric, ferroelectric, and piezoelectric investigation of polymer-Based P(VDF-TrFE) Composites *Phys. Status Solidi* **255**
[96] Samet M, Boiteux G, Seytre G, Kallel A and Serghei A 2014 Interfacial polarization in composite materials with spherical fillers: characteristic frequencies and scaling laws *Colloid Polym. Sci.* **292** 1977–88
[97] Myroshnychenko V, Mulavarickal Jose P M, Farheen H, Ejaz S, Brosseau C and Förstner J 2024 From Swiss-cheese to discrete ferroelectric composites: assessing the ferroelectric butterfly shape in polarization loops *Phys. Scr.* **99** 045952
[98] Padurariu L, Brunengo E, Canu G, Curecheriu L P, Conzatti L, Buscaglia M T, Stagnaro P, Mitoseriu L and Buscaglia V 2023 Role of microstructures in the dielectric properties of PVDF-based nanocomposites containing high-permittivity fillers for energy storage *ACS Appl. Mater. Interfaces* **15** 13535–44
[99] Feng Y, Li W L, Hou Y F, Yu Y, Cao W P, Zhang T D and Fei W D 2015 Enhanced dielectric properties of PVDF-HFP/$BaTiO_3$ -nanowire composites induced by interfacial polarization and wire-shape *J. Mater. Chem. C* **3** 1250–60
[100] Samet M, Levchenko V, Boiteux G and Seytre G Kallel A and Serghei A 2015 Electrode polarization vs. Maxwell-Wagner-Sillars interfacial polarization in dielectric spectra of materials: characteristic frequencies and scaling laws *J. Chem. Phys.* **142**

[101] Hussein M M, Saafan S A, Abosheiasha H F, Kamal A A, Mahmoud A E, Zhou D, Trukhanov S V, Zubar T I, Trukhanov A V and Darwish M A 2023 Structural and dielectric characterization of synthesized nano-BSTO/PVDF composites for smart sensor applications *Mater. Adv.* **4** 5605–17
[102] Jin L, Li F and Zhang S 2014 Decoding the fingerprint of ferroelectric loops: comprehension of the material properties and structures ed DJ green *J. Am. Ceram. Soc.* **97** 1–27
[103] Su Y, Chen C, Wang Y, Yao M, Ma R, Zhang W, Yuan Q and Hu D 2022 Interface coupling and energy storage of inorganic–organic nanocomposites *J. Mater. Chem. A* **10** 14187–220
[104] Ma F D and Wang Y U 2015 Depolarization field effect on dielectric and piezoelectric properties of particulate ferroelectric ceramic-polymer composites *J. Appl. Phys.* **117** 124101
[105] Sihvola A 2007 Dielectric polarization and particle shape effects *J. Nanomater.* **2007** 1–9
[106] Kannan V, Trassin M and Kochmann D M 2022 Kinetics of ferroelectric switching in poled barium titanate ceramics: effects of electrical cycling rate *Materialia* **25** 101553
[107] Chilton J A 1995 *Electroactive Composites Special Polymers for Electronics and Optoelectronics* (Springer) pp 221–55
[108] Ikei A, Wissman J, Sampath K, Yesner G and Qadri S N 2021 Tunable *In Situ* 3D-Printed PVDF-TrFE piezoelectric arrays *Sensors* **21** 5032